SANDIA REPORT

SAND2013-0369
Unlimited Release
Printed January 2013

Elucidating the Role of Interfacial Materials Properties in Microfluidic Packages

Thayne L. Edwards

Prepared by
Sandia National Laboratories
Albuquerque, New Mexico 87185 and Livermore, California 94550

Sandia National Laboratories is a multi-program laboratory managed and operated by Sandia Corporation, a wholly owned subsidiary of Lockheed Martin Corporation, for the U.S. Department of Energy's National Nuclear Security Administration under contract DE-AC04-94AL85000.

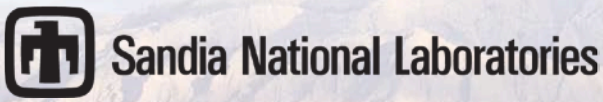

Issued by Sandia National Laboratories, operated for the United States Department of Energy by Sandia Corporation.

Available to DOE and DOE contractors from
U.S. Department of Energy
Office of Scientific and Technical Information
P.O. Box 62
Oak Ridge, TN 37831

Telephone: (865) 576-8401
Facsimile: (865) 576-5728
E-Mail: reports@adonis.osti.gov
Online ordering: http://www.osti.gov/bridge

Available to the public from
U.S. Department of Commerce
National Technical Information Service
5285 Port Royal Rd.
Springfield, VA 22161

Telephone: (800) 553-6847
Facsimile: (703) 605-6900
E-Mail: orders@ntis.fedworld.gov
Online order: http://www.ntis.gov/help/ordermethods.asp?loc=7-4-0#online

SAND2013-0369
Unlimited Release
Printed January 2013

Elucidating the Role of Interfacial Materials Properties in Microfluidic Packages

Thayne L. Edwards
Biosensors and Nanomaterials Department
Sandia National Laboratories
P.O. Box 5800
Albuquerque, New Mexico 87185-MS0892

Abstract

The purpose of this work was to discover a method to investigate the properties of interfaces as described by a numerical physical model. The model used was adopted from literature and applied to a commercially available multiphysics software package. By doing this the internal properties of simple structures could be elucidated and then readily applied to more complex structures such as valves and pumps in laminate microfluidic structures.

A numerical finite element multi-scale model of a cohesive interface comprised of heterogeneous material properties was used to elucidate irreversible damage from applied strain energy. An unknown internal state variable was applied to characterize the damage process. Using a constrained blister test, this unknown internal state variable could be determined for an adherend/adhesive/adherend body. This is particularly interesting for laminate systems with microfluidic and microstructures contained within the body. A laminate structure was designed and fabricated that could accommodate a variety of binary systems joined using nearly any technique such as adhesive, welding (solvent, laser, ultrasonic, RF, etc.), or thermal. The adhesive method was the most successful and easy to implement but also one of the more difficult to understand, especially over long periods of time. Welding methods are meant to achieve a bond that is similar to bulk properties and so are easier to predict. However, methods of welding often produce defects in the bonds..

Examples of the test structures used to elucidate the internal properties of the model were shown and demonstrated. The real life examples used this research to improve upon current designs and aided in creating complex structures for sensor and other applications.

CONTENTS

FIGURES

NOMENCLATURE

DOE	Department of Energy
SNL	Sandia National Laboratories
PET	poly-ethylene terapthalate
PMMA	poly-methyl mythacrylate
mil	milli-inch (0.001 inches)
CAD	Computer Aided Drawing
CO_2 Laser	Carbon Dioxide Laser
PEU	poly-ether urethane
PE	poly-ethylene

1. INTRODUCTION

1.1. Motivation for Work

Microsensors for chemical and biological detection have seen relatively little field application because the small size and low cost of the microsensor are offset by the large size, high cost, and complexity of the balance of the sensing system – principally, the required external pumps and valves. Attempts have been made to integrate these components into the sensor's microfluidic package but success has been limited by the lack of software design tools to simulate microfluidic device performance and the high cost of design-by-intuition and trial-and-error methods. Software simulation, in turn, is limited by in part by our lack of understanding of the materials properties at the interfaces comprising the package and sensor itself. It is also limited to many researchers due to the lack of computing power for these sensors that typically apply to scales from nano to macro (approximately 10^{-9} m to 10^{-1} m). Multiscale, multiphysical, and heterogeneous (material properties) models require creative and custom approaches that can be very time intensive and expensive.

Beside the issue of integration of external components are other issues associated with packaging the sensor such as material compatibility, microfluidics, and longevity, to name a few. A number of technologies have been employed to create microfluidic packages for microsensors, including silicon and glass micromachining, ceramic laminates, plastic injection molding, hot embossing, and cast molding, and plastic laminates. Of these, plastic laminate packaging provides an attractive combination of low capital and material cost, rapid prototyping, and complex mechanical and fluidic structures. This technology employs a variety of thin polymer and metal films bonded by adhesives, solvents, thermal fusion, and ultrasonic welding. The properties of these interfaces – thermal and electrical conductivity, mechanical deformation, adhesion strength, and chemical resistance – vary from the bulk properties of the laminate films and depend on the laminate composition and joining method employed.

1.2. Interfacial Properties Investigation

This research addressed these shortcomings by: 1) designing experiments to extract the relevant mechanical, thermal, electrical, and chemical properties of plastic laminate interfaces; 2) developing a multiphysics model incorporating these parameters for plastic laminate microfluidic devices; and 3) demonstrating the model's capabilities by designing, fabricating, and testing a microfluidic valve. Plastics will be the primary materials under investigation but these methods are expected to apply to other materials as well.

Several plastic joining methods were investigated such as adhesives, solvent welding, laser welding, and ultrasonic welding. The adhesive method has been used in the past for packaging sensors and has shown to be the most successful and easy to implement. This method is also complicated by heterogeneous and sometimes non uniform properties making it difficult to ensure repeat performance. The welding methods are meant to achieve a bond that is similar to bulk properties and so are easier to predict but usually apply only to joining the same material or two very similar materials. Additionally, these methods of welding often produce defects in the bonds and may locally modify material properties from the thermal processes.

These defects and complex adhesives require a physical model that is heterogeneous on the microscale. This presents complications for numerical models due to the multiple scales over which the structures are being investigated. Again literature has aided in the solution of this and the model used included a repetitive volume element and multiscale model to reduce the computing power required.

1.3. Description of Approach

This work will revolve around a test structure built using the laminate technology that has been previously employed to successfully create sensor packages. A cross section of this structure is shown in Figure 1. In this schematic the main structure is shown at the top where the interface

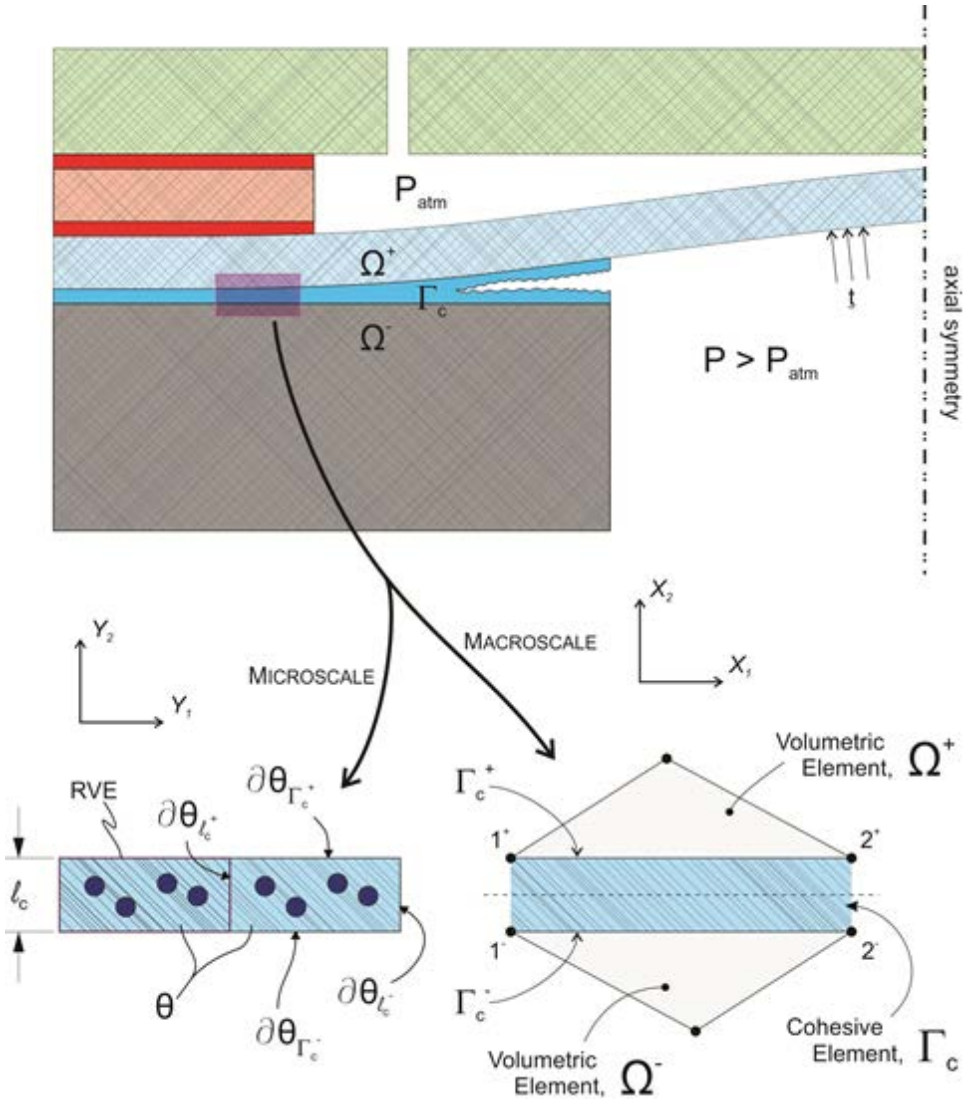

Figure 1. Description of physical model including multiple scale coordinate systems, critical dimensions and forces, and the repetitive volume element of the heterogeneous cohesive layer.

under investigation is in blue. The interface is joining the light blue hatched and the dark grey hatched structures. The light blue hatched is designed to flex which the grey is fixed. The green hatched is a constraint layer used to control the experiment energy and limit it to the fracture of the interface and not the in other processes such as strain energy. The purpose of the red layer is geometry control. Because gas pressure is used for the driving force the traction vectors are always normal to the flexible membrane. This method is referred to as a constrained blister test and will utilize the theory behind it to understand the physical nature of the interface.

The theory of the interface as applied to a numerical finite element model is broken down into two scales to conserve processing power. The macroscale follows typical finite element model processes. The microscale contains the information of interest. It's properties are approximated using a repetitive volume element (RVE), averaged over the area, and mapped to the macroscale nodes. The RVE may contain either a homogeneous or heterogeneous composition. Damage in this layer is also accounted for by use of an internal energy variable with a threshold damage parameter. This internal variable is estimated by the constrained blister test.

The theory of the multiscale model, heterogeneous repetitive volume element, and damage parameter are first explained with limited wording. If additional information is necessary then the author suggests reading the related work.[1-6] This is followed by the theory of the blister test and in particular the constrained blister test. The experimental section describes the actual test structure and the joining methods used to create the interfaces under test. It also shows the results of the joining methods and some of the results of the constrained blister test with one example of determining the energy released for delamination. This work is then summarized in the conclusion.

2. THEORY OF MODEL

2.1. Description of Theory

The basis of the theory follows that of Matous et al.[1] wherein was described a multiscale cohesive model for heterogeneous adhesives. This theory was used in this work to describe any heterogeneous interface used to join two adherends with uniform and homogeneous material properties. The theory begins with a description, mathematically, of the space, dimensions, body, and submanifolds as well as the mechanical components of the boundary value problem to be solved. The mechanical boundary value problem is then described, which is common to continuum mechanical models and reiterated here. Following this problem description is the model relating the macro properties of the heterogeneous cohesive layer to the micro-scale properties of the same. The macro-scale properties of the cohesive layer is then coupled to that of the adherends and discretized and linearized to put the equations into a finite element model to be solved.

2.2. Mathematical Description of Body

Body: $\Omega \subset \mathbb{R}^{\Re}$

Material Points: $\boldsymbol{X} \in \mathbb{R}^{\Re}$

Space Dimension: $\Re$

Boundary: $\partial\Omega = \partial\Omega_u \cap \partial\Omega_t$ and $\partial\Omega_u \cap \partial\Omega_t = \emptyset$

Prescribed Displacement: $\bar{\boldsymbol{u}}$

Prescribed Traction: $\bar{\boldsymbol{t}}$

Sub-manifold (heterogeneous adhesive layer): Γ_c

Material Points: $\boldsymbol{X} \in \mathbb{R}^{\Re}$

Space Dimension: $\Re - 1$

Unit Normal: $\boldsymbol{N}(\boldsymbol{X})$

Characteristic (effective) thickness: $l_c = \frac{\Psi}{\Gamma_c} > 0$

Volume (or Area) of Adhesive Layer: $\Psi = \int_{\Psi} d\Psi$

Local periodicity: $Y_{1,2}$ – periodic and in-plane Γ_c – periodic

Microstructure periodicity defined by Representative Volume Element (RVE): θ

Sub-bodies (adherends): $\Omega = \Omega^+ \cup \Omega^- \cup \Psi$

Where Ω^+ and Ω^- are associated with the cohesive surface sides, Γ_c^+ and Γ_c^-, respectively.

2.3. Governing Equations

Basic mechanics of continuum model is described here:
Starting from the Newton's second law (in the form of the general momentum balance equation)

$$\boldsymbol{f} + \nabla \cdot \boldsymbol{\sigma} = \rho \frac{d^2 \boldsymbol{u}}{dt^2}.$$

Multiply by velocity field and integrate over volume

$$\int_V (v \cdot \boldsymbol{f} + v \cdot \nabla \cdot \boldsymbol{\sigma})\, dV = \int_V v \cdot \rho \frac{d^2 u}{dt^2}\, dV$$

or

$$\int_V (v \cdot \boldsymbol{f} + v \cdot \nabla \cdot \boldsymbol{\sigma})\, dV = \underbrace{\int_V \frac{\rho}{2} \frac{dv^2}{dt}\, dV}_{\frac{dKE}{dt}}$$

The right hand side is the time rate change of kinetic energy. The left side contains the stored strain energy. It is extracted using the identity

$$\nabla \cdot (v \cdot \boldsymbol{\sigma}) = \nabla v : \boldsymbol{\sigma} + v \cdot \nabla \cdot \boldsymbol{\sigma}$$

The momentum balance equation becomes

$$\frac{dKE}{dt} = \int_V (v \cdot \boldsymbol{f} + \nabla \cdot (v \cdot \boldsymbol{\sigma}) - \nabla v : \boldsymbol{\sigma}) dV$$

Using the divergence theorem[1] on the second term on the right the momentum balance becomes

$$\frac{dW}{dt} = \frac{dKE}{dt} + \frac{dU}{dt} = \int_V v \cdot \boldsymbol{f}\, dV + \int_S v \cdot \boldsymbol{t}\, dS$$

where

$$\boldsymbol{t} = \boldsymbol{\sigma} \cdot n$$

are the surface traction forces and

$$\frac{dU}{dt} = \int_V \nabla v : \boldsymbol{\sigma}\, dV$$

is the internal energy of the system. The vector field in this term can be separated into rotational and non-rotation components using

$$\nabla v = \underbrace{\frac{1}{2}[\nabla v + (\nabla v)^T]}_{\substack{\text{symmetric gradient} \\ \text{operator}, \nabla^S}} + \underbrace{\frac{1}{2}[\nabla v - (\nabla v)^T]}_{\substack{\text{rotational} \\ \text{component}}}$$

The rotation component operated on the stress will be zero since it is antisymmetric. Furthermore, since the velocity is the time rate change of position,

$$\nabla v = \frac{1}{2}[\nabla v + (\nabla v)^T] = \frac{1}{2}\left[\nabla \frac{du}{dt} + \left(\nabla \frac{du}{dT}\right)^T\right] = \frac{d}{dt}\left\{\frac{1}{2}[\nabla \boldsymbol{u} + (\nabla \boldsymbol{u})^T]\right\} = \frac{d\varepsilon}{dt}$$

[1] Divergence theorem: $\iiint_V (\nabla \cdot F) dV = \oiint_S (F \cdot n) dS$

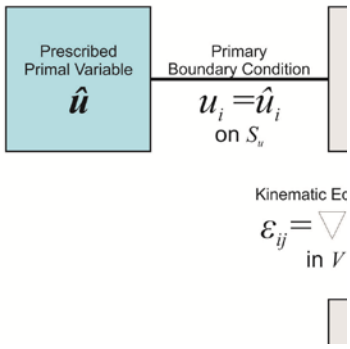

Figure 2. Relationships between equations and variables of the mechanical envelope.

Problem specific:

Displacement field in the adhesive layer: ${}^{A}\boldsymbol{u}(\boldsymbol{X},\boldsymbol{Y}) = {}^{0}\boldsymbol{u}(\boldsymbol{X}) + {}^{1}\boldsymbol{u}(\boldsymbol{Y})$

Macroscopic displacement: ${}^{0}\boldsymbol{u}(\boldsymbol{X})$

Microscopic fluctuation displacement: ${}^{1}\boldsymbol{u}(\boldsymbol{Y})$

Displacement field space

$$\mathcal{V}_{\Psi\times\Theta} = \left\{ \begin{array}{c} {}^{A}\boldsymbol{u}(\boldsymbol{X},\boldsymbol{Y}) \mid {}^{A}\boldsymbol{u}(\boldsymbol{X},\boldsymbol{Y}) \in [H^1(\Psi)\times L^2(\Psi;\, V_\Theta)]^{\mathfrak{R}}, \\ {}^{1}\boldsymbol{u}(\circ,\boldsymbol{Y}) \; is \; Y_{1,2} - periodic \\ {}^{A}\boldsymbol{u}(\circ,\boldsymbol{Y})|_{\Gamma_\sigma^\pm} = {}^{0}\boldsymbol{u}(\boldsymbol{X}) \end{array} \right\}$$

2.4. Boundary Value Problem

Adherends (all defined in regions, $\Omega^{\pm}$):

$$\nabla \cdot \boldsymbol{\sigma}(\boldsymbol{X}) + \boldsymbol{f}(\boldsymbol{X}) = 0$$
$$\boldsymbol{\sigma}(\boldsymbol{X}) = \boldsymbol{L}(\boldsymbol{X}) : \boldsymbol{\varepsilon}(\boldsymbol{X})$$
$$\boldsymbol{\varepsilon}(\boldsymbol{X}) = \nabla_{\boldsymbol{X}}^{S}\boldsymbol{u}(\boldsymbol{X})$$

Adhesive (all defined in region, Ψ):

$$\nabla \cdot \boldsymbol{\tau}(\boldsymbol{Y}) = 0$$
$$\boldsymbol{\tau}(\boldsymbol{Y}) = \mathbb{L}(\boldsymbol{X},\boldsymbol{Y}) : [{}^{0}\boldsymbol{\varepsilon}(\boldsymbol{X}) + {}^{1}\boldsymbol{\varepsilon}(\boldsymbol{Y})]$$
$${}^{0}\boldsymbol{\varepsilon}(\boldsymbol{X}) = \nabla_{\boldsymbol{X}}^{S}\, {}^{0}\boldsymbol{u}(\boldsymbol{X})$$
$${}^{1}\boldsymbol{\varepsilon}(\boldsymbol{Y}) = \nabla_{\boldsymbol{Y}}^{s}\, {}^{1}\boldsymbol{u}(\boldsymbol{Y})$$

Boundary conditions (defined on surfaces specified):

$\boldsymbol{N} \cdot \boldsymbol{\sigma}|_{\Gamma_\sigma^\pm} + \boldsymbol{N} \cdot \boldsymbol{\tau}|_{\Gamma_\sigma^\pm} = 0$ on surfaces, $\Gamma_\sigma^\pm$

$\boldsymbol{\sigma}(\boldsymbol{X}) \cdot \boldsymbol{n}(\boldsymbol{X}) = \bar{\boldsymbol{t}}(\boldsymbol{X})$ on surface, $\partial\Omega_t$

$\boldsymbol{u}(\boldsymbol{X}) = \bar{\boldsymbol{u}}(\boldsymbol{X})$ on surface, $\partial\Omega_u$

Definitions:

Divergence operator: $\nabla \cdot$

$$\nabla \cdot \boldsymbol{\sigma} \equiv \sigma_{ij,j} = \sum_{j=1}^{3} \frac{\partial \sigma_{ij}}{\partial x_j} = \begin{bmatrix} \left(\frac{\partial \sigma_{11}}{\partial x_1} + \frac{\partial \sigma_{12}}{\partial x_2} + \frac{\partial \sigma_{13}}{\partial x_3}\right) \\ \left(\frac{\partial \sigma_{21}}{\partial x_1} + \frac{\partial \sigma_{22}}{\partial x_2} + \frac{\partial \sigma_{23}}{\partial x_3}\right) \\ \left(\frac{\partial \sigma_{31}}{\partial x_1} + \frac{\partial \sigma_{32}}{\partial x_2} + \frac{\partial \sigma_{33}}{\partial x_3}\right) \end{bmatrix}$$

Stress tensor in adherend spaces, $\Omega^{\pm}$: $\boldsymbol{\sigma}(\boldsymbol{X})$
Body force vector: $\boldsymbol{f}(\boldsymbol{X})$
Symmetric material tensor for homogenous adherend: $\boldsymbol{L}(\boldsymbol{X})$
Strain tensor in adherend spaces, $\Omega^{\pm}$: $\boldsymbol{\varepsilon}(\boldsymbol{X})$
Symmetric gradient operators with respect to $\boldsymbol{X}$ and $\boldsymbol{Y}$ coordinates: ∇_X^S, ∇_Y^S. [Note 2]

$$\nabla_X^S \cdot \boldsymbol{u}(\boldsymbol{X}) = \frac{1}{2}(\nabla + \nabla^T) \cdot \boldsymbol{u}(\boldsymbol{X}) = \begin{bmatrix} \frac{\partial}{\partial x_1} & 0 & 0 \\ 0 & \frac{\partial}{\partial x_2} & 0 \\ 0 & 0 & \frac{\partial}{\partial x_3} \\ 0 & \frac{\partial}{\partial x_3} & \frac{\partial}{\partial x_2} \\ \frac{\partial}{\partial x_3} & 0 & \frac{\partial}{\partial x_1} \\ \frac{\partial}{\partial x_2} & \frac{\partial}{\partial x_1} & 0 \end{bmatrix} \begin{bmatrix} u_1 \\ u_2 \\ u_3 \end{bmatrix} = \begin{bmatrix} \frac{\partial u_1}{\partial x_1} \\ \frac{\partial u_2}{\partial x_2} \\ \frac{\partial u_3}{\partial x_3} \\ \frac{\partial u_3}{\partial x_2} + \frac{\partial u_2}{\partial x_3} \\ \frac{\partial u_1}{\partial x_3} + \frac{\partial u_3}{\partial x_1} \\ \frac{\partial u_2}{\partial x_1} + \frac{\partial u_1}{\partial x_2} \end{bmatrix}$$

Stress tensor in adhesive space: $\boldsymbol{\tau}(\boldsymbol{X}, \boldsymbol{Y})$
Spatially dependent instantaneous secant stiffness tensor of the interface: $\mathbb{L}(\boldsymbol{X}, \boldsymbol{Y})$
Macroscopic strain tensor in the adhesive layer: ${}^0\boldsymbol{\varepsilon}(\boldsymbol{X})$
Microscopic strain tensor in the adhesive layer: ${}^1\boldsymbol{\varepsilon}(\boldsymbol{Y})$

2.5. Space Dimension Reduction

(cohesive layer kinematics to approximate ${}^0\boldsymbol{\varepsilon}$)

In-plane components (an average of the displacements of the top and bottom adherends):

$${}^0\varepsilon_{11} = \nabla_{X_1}^S {}^0u_1 \approx \frac{1}{2}\left(\nabla_{X_1}^S {}^0u_1^+ + \nabla_{X_1}^S {}^0u_1^-\right)$$

$${}^0\varepsilon_{22} = \nabla_{X_2}^S {}^0u_1 \approx \frac{1}{2}\left(\nabla_{X_2}^S {}^0u_2^+ + \nabla_{X_2}^S {}^0u_2^-\right)$$

[2] Only the symmetric gradient operator is necessary.

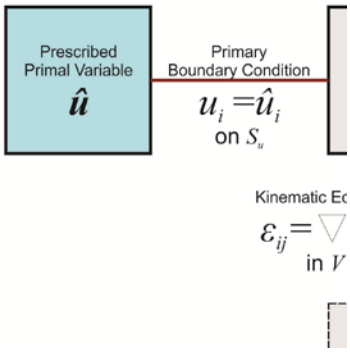

Figure 3. Reduced form of the mechanical envelope.

$$ {}^0\varepsilon_{12} = {}^0\varepsilon_{21} = \frac{1}{2}\left(\nabla^S_{X_2}\,{}^0u_1 + \nabla^S_{X_1}\,{}^0u_2\right) \approx \frac{1}{2}\left(\frac{1}{2}\left(\nabla^S_{X_2}\,{}^0u_1^+ + \nabla^S_{X_2}\,{}^0u_1^-\right) + \frac{1}{2}\left(\nabla^S_{X_1}\,{}^0u_2^+ + \nabla^S_{X_1}\,{}^0u_2^-\right)\right) $$

Out-of-plane components (an average of the thickness of the adhesive layer):

$$ {}^0\varepsilon_{33} \approx \frac{1}{l_c}\left({}^0u_3^+ - {}^0u_3^-\right) = \frac{1}{l_c}\left[{}^0u_3\right] $$

$$ {}^0\varepsilon_{13} = {}^0\varepsilon_{31} \approx \frac{1}{2l_c}\left({}^0u_1^+ - {}^0u_1^-\right) = \frac{1}{2l_c}\left[{}^0u_1\right] $$

$$ {}^0\varepsilon_{23} = {}^0\varepsilon_{32} \approx \frac{1}{2l_c}\left({}^0u_2^+ - {}^0u_2^-\right) = \frac{1}{2l_c}\left[{}^0u_2\right] $$

Jump operator: $\left[\blacksquare\right] = \blacksquare^+ - \blacksquare^-$

The strain

$$ {}^0\boldsymbol{\varepsilon} \equiv \frac{1}{l_c}\left[\left[{}^0\boldsymbol{u}\right]\right] = \frac{1}{l_c}\begin{bmatrix} l_c\,{}^0\varepsilon_{11} & l_c\,{}^0\varepsilon_{12} & \frac{1}{2}\left[{}^0u_1\right] \\ l_c\,{}^0\varepsilon_{21} & l_c\,{}^0\varepsilon_{22} & \frac{1}{2}\left[{}^0u_2\right] \\ \frac{1}{2}\left[{}^0u_1\right] & \frac{1}{2}\left[{}^0u_2\right] & \left[{}^0u_3\right] \end{bmatrix} $$

Out-of-plane dominates *in-plane* components, so the *in-plane* can be neglected.

$$ \gamma_{ij} = 2\varepsilon_{ij}, \forall\ (i \neq j) $$

Using standard variational methods (SVM, see Tonti diagram) the boundary value problem becomes

$$ \int_{\Omega^\pm} \boldsymbol{\sigma} : \nabla^s_X \delta\boldsymbol{u}\ \mathrm{d}\Omega + \int_{\Psi} \boldsymbol{\tau} : \nabla^s_X \delta\boldsymbol{u}\ \mathrm{d}\Psi - \int_{\Omega^\pm} \boldsymbol{f} \cdot \delta\boldsymbol{u}\ \mathrm{d}\Omega - \int_{\partial\Omega_t} \bar{\boldsymbol{t}} \cdot \delta\boldsymbol{u}\ \mathrm{dA} = 0 $$

for all admissible variations $\delta\boldsymbol{u}$ satisfying

$$ \mathcal{V} = \left\{\delta\boldsymbol{u} | \delta\boldsymbol{u} \in \left[H^1(\Omega)\right]^{\Re}\right\}, \delta\boldsymbol{u} = 0\ on\ \partial\Omega_u. $$

The first term and second terms are for the adherend and adhesive, respectively. Regarding the adhesive term, integrating by parts, applying the divergence theorem, and approximating the volume integral with an area integral multiplied by the thickness,

$$\int_{\Psi} \blacksquare \, d\Psi \approx \; l_c \int_{\Gamma_c} \blacksquare \, dA,$$

it becomes

$$\int_{\Psi} \boldsymbol{\tau} : \nabla_X^S \delta \boldsymbol{u} \, d\Psi = \left\{ \overbrace{-l_c \int_{\Gamma_c} \nabla_X^s \cdot \boldsymbol{\tau} \cdot \delta \boldsymbol{u} \, dA}^{\text{comparatively small}} + \int_{\partial\Psi} \boldsymbol{N} \cdot \boldsymbol{\tau} \cdot \delta \boldsymbol{u} \, dA \right\} \approx \left\{ 0 + \int_{\Gamma_c} \boldsymbol{t} \cdot [\delta^0 \boldsymbol{u}] \, dA \right\}$$

The first term is neglected since the thickness is assumed to be very small relative to other dimensions. The second term is assumed to have no external forces acting on the boundary, $\partial\Theta_{l_c^{\pm}}$, of the adhesive bond line, only cohesive traction forces. The implication is that this equation equals zero as the thickness approaches zero and yields the classical cohesive contribution to the principal of virtual work,

$$\underbrace{\int_{\Omega^{\pm}} \boldsymbol{\sigma} : \nabla_X^S \delta^0 \boldsymbol{u} \, d\Omega}_{\text{volumetric}} + \underbrace{\int_{\Gamma_c} \boldsymbol{t} \cdot [\delta^0 \boldsymbol{u}] \, dA}_{\text{cohesive}} - \int_{\Omega^{\pm}} \boldsymbol{f} \cdot \delta^0 \boldsymbol{u} \, d\Omega - \int_{\partial\Omega_t} \bar{\boldsymbol{t}} \cdot \delta^0 \boldsymbol{u} \, dA = 0,$$

where the first term is the volumetric contribution and the second term is the cohesive contribution for all admissible variations $\delta^0 \boldsymbol{u}$ satisfying

$$\mathcal{V} = \{\delta \boldsymbol{u} | \delta \boldsymbol{u} \in [H^1(\Omega)]^{\Re}\}, \delta^0 \boldsymbol{u} = 0 \; on \; \partial\Omega_u,$$

and where

$$\delta \boldsymbol{u} = \delta^0 \boldsymbol{u}(\boldsymbol{X})$$

due to the weighting functions being arbitrary and belong to the spaces of bounded variations as they are discontinuous across the interface.

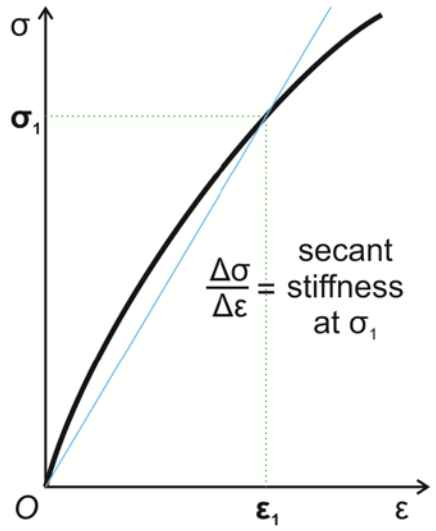

Figure 4. Typical stress strain curve of an elastic material and the associated secant stiffness coefficient at a particular strain.

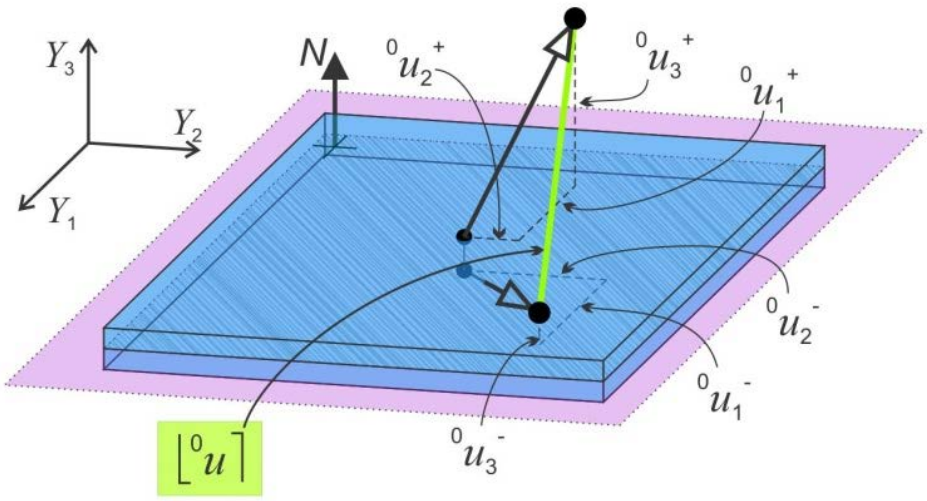

Figure 5. Definition of the displacement vector of the jump operator and normal vector relative to the mechanical manifold.

2.4. Macroscale Deformation Effects on Microscale Deformation

Scale separation theory dictates

$$\frac{l_{micro}}{l_{macro}} \ll 1,$$

with characteristic lengths,

$l_{micro} \approx \mathcal{O}(\Gamma_c)$, (i.e., the thickness of the adherend)

$l_{macro} \approx \mathcal{O}(l_c)$, (i.e., the thickness of the adhesive)

Potential energy at a point in a material is minimized on the macro and micro scales when the following condition of stationarity (Hill's lemma) is satisfied:

$$\underbrace{\inf \underline{\psi}(\lfloor {}^0\boldsymbol{u} \rceil)}_{\text{microscale}} = \underbrace{\inf \inf \frac{1}{|\Theta|} \int_\Theta \psi({}^0\varepsilon(\lfloor {}^0\boldsymbol{u} \rceil) + \nabla_Y^S {}^1\boldsymbol{u})\, d\Theta}_{\text{macroscale}}$$

and

$${}^0\boldsymbol{\varepsilon}(\lfloor {}^0\boldsymbol{u} \rceil) \in \mathfrak{Q}^+,$$

$${}^1\boldsymbol{u} \in \mathcal{r}_\Theta .$$

Definitions

ψ – free energy density on the **micro**-scale

$\underline{\psi}$ – free energy density on the **macro**-scale

$\mathfrak{L}^{+}$ - space of second order tensors with positive determinant

Coleman and Noll's method of relating the stress to the free energy density on the micro-scale (ψ) and relating the tractions to the homogenized free energy density on the macro-scale ($\underline{\psi}$) yield the following constitutive laws:

$$\boldsymbol{\tau} = \frac{\partial \psi}{\partial {}^{A}\boldsymbol{\varepsilon}}$$

$$\boldsymbol{t} = \frac{\partial \underline{\psi}}{\partial [{}^{0}\boldsymbol{u}]}$$

where the strain in the adhesive layer is given by, ${}^{A}\boldsymbol{\varepsilon} = {}^{0}\boldsymbol{\varepsilon} + {}^{1}\boldsymbol{\varepsilon}$.

Using standard variational principles to get the variational energy condition,

$$\mathcal{R}_{[{}^{0}\boldsymbol{u}]} = \left[N \cdot \left(\frac{1}{|\Theta|}\int_{\Theta} \tau \, d\Theta\right) - t\right] \cdot [\delta^{0}\boldsymbol{u}] = 0$$

$$\mathcal{R}_{{}^{1}\boldsymbol{u}} = \frac{1}{|\Theta|}\int_{\Theta} \tau : \nabla_{Y}^{S} \delta^{1}\boldsymbol{u} \, d\Theta = 0$$

and

$$\delta^{1}\boldsymbol{u} \in [H^{1}(\Theta)]^{\Re},$$

$$\delta^{1}\boldsymbol{u}|_{\partial\Theta_{\Gamma_C^{+}}} = 0,$$

$$\delta^{1}\boldsymbol{u} = \text{periodic} \qquad \text{on } \partial\Theta_{l_C^{\pm}},$$

where

$$\partial\Theta = \partial\Theta_{\Gamma_C^{+}} \cup \partial\Theta_{l_C^{+}} \cup \partial\Theta_{\Gamma_C^{-}} \cup \partial\Theta_{l_C^{-}}$$

is the boundary of the RVE, Θ. Since the displacement jump variation is arbitrary it is convenient to use,

$$\delta^{0}\boldsymbol{\varepsilon}([\delta^{0}\boldsymbol{u}]) = \frac{1}{l_C}\boldsymbol{N} \otimes [\delta^{0}\boldsymbol{u}],$$

where $\otimes$ represents the dyadic vector product or tensor product.

Observations from these equations include:

1. The volume average of the variation of the work performed on the RVE equals the local variation of the work on the macro-scale,
2. The micro-scale fluctuation field does not contribute to the average variation of the work and,

3. The macroscopic tractions are equal to the volume average of the stress at the micro-scale contracted with the normal due to the arbitrariness of the macro-scale displacement jump vector, $[\![\delta^0\boldsymbol{u}]\!]$.
4. These equations are generally non-linear based on individual constituent mechanical behaviors including inelastic processes such as plasticity, nonlinear viscoelasticity, and damage. These processes are expressed in the secant stiffness tensor, $\mathbb{L}(\boldsymbol{X},\boldsymbol{Y})$.

To define the potential free energy density in Hill's lemma and constitutive laws for macro-scale traction and stress the following assumptions are made:

1. Neglect thermal effects
2. The elastic potential is not dependent on the inelastic process
3. Elastic processes are linear and elastic strains are small

$$\psi({}^A\boldsymbol{\varepsilon}) = \frac{1}{2}({}^0\boldsymbol{\varepsilon}+{}^1\boldsymbol{\varepsilon}):\mathbb{L}:({}^0\boldsymbol{\varepsilon}+{}^1\boldsymbol{\varepsilon})$$

$$\boldsymbol{\tau} = \frac{\partial\psi}{\partial^A\boldsymbol{\varepsilon}} = \mathbb{L}:[{}^0\boldsymbol{\varepsilon}+{}^1\boldsymbol{\varepsilon}]$$

$$\boldsymbol{t} = \begin{bmatrix}\boldsymbol{t_1}\\ \boldsymbol{t_2}\\ \boldsymbol{t_n}\end{bmatrix} = \boldsymbol{N}\cdot\left\{\frac{1}{|\mathcal{B}|}\int_{\mathcal{B}}\mathbb{L}:\left[\frac{1}{l_c}\right][\![[\![{}^0\boldsymbol{u}]\!]]\!] + \nabla_Y^s\,{}^1\boldsymbol{u}\,\mathrm{d}\Theta\right\}$$

For a homogenous adhesive layer, where $\mathbb{L}(\boldsymbol{X},\boldsymbol{Y}) = \mathbb{L}(\boldsymbol{X})$,

$$\boldsymbol{t} = \frac{1}{l_c}\boldsymbol{N}\cdot\{\mathbb{L}:[\![[\![{}^0\boldsymbol{u}]\!]]\!]\},$$

$$\frac{1}{|\mathcal{B}|}\int_{\mathcal{B}}\nabla_Y^s\,{}^1\boldsymbol{u}\,\mathrm{d}\Theta = 0 \Longrightarrow \frac{1}{|\mathcal{B}|}\int_{\partial\mathcal{B}}\frac{1}{2}[\boldsymbol{N}_{\mathcal{B}}\otimes{}^1\boldsymbol{u} + {}^1\boldsymbol{u}\otimes\boldsymbol{N}_{\mathcal{B}}]\mathrm{d}A = 0.$$

$\boldsymbol{N}_{\mathcal{B}}$ – Outward Normal of the micro-system at $\boldsymbol{Y}\in\partial\Theta$ (Note: $\forall\,\boldsymbol{Y}\in\partial\Theta_{\Gamma_c^+}, \boldsymbol{N}_{\mathcal{B}}\equiv\boldsymbol{N}$.

Linearization of macroscopic traction-separation law

To get the linearized form of the macroscopic traction-separation law, need to linearize:

$$\mathcal{R}_{[\![{}^0\boldsymbol{u}]\!]} = \left[N\cdot\left(\frac{1}{|\mathcal{B}|}\int_{\mathcal{B}}\tau\,d\Theta\right) - t\right]\cdot[\![\delta^0\boldsymbol{u}]\!] = 0$$

$$\mathcal{R}_{{}^1\boldsymbol{u}} = \frac{1}{|\mathcal{B}|}\int_{\mathcal{B}}\tau:\nabla_Y^s\delta^1\boldsymbol{u}\,d\Theta = 0$$

which becomes,

$$\begin{bmatrix}\mathcal{K}_{11} & \mathcal{K}_{12}\\ \mathcal{K}_{21} & \mathcal{K}_{22}\end{bmatrix}^k = \begin{Bmatrix}[\![\Delta^0\boldsymbol{u}]\!]\\ \Delta^1\boldsymbol{u}\end{Bmatrix} = \begin{Bmatrix}\boldsymbol{t}\\ \boldsymbol{0}\end{Bmatrix}^{k+1} - \begin{Bmatrix}\boldsymbol{t}\\ \boldsymbol{\mathcal{R}}_2\end{Bmatrix}^k,$$

where,

$$[\delta^0 \boldsymbol{u}] \cdot \mathcal{K}_{11} \equiv \frac{\partial \mathcal{R}_{[^0u]}}{\partial [^0 \boldsymbol{u}]},$$

$$[\delta^0 \boldsymbol{u}] \cdot \mathcal{K}_{12} \equiv \frac{\partial \mathcal{R}_{[^0u]}}{\partial {}^1\boldsymbol{u}},$$

$$\delta^1 \boldsymbol{u} \cdot \mathcal{K}_{21} \equiv \frac{\partial \mathcal{R}_{^1u}}{\partial [^0 \boldsymbol{u}]},$$

$$\delta^1 \boldsymbol{u} \cdot \mathcal{K}_{22} \equiv \frac{\partial \mathcal{R}_{^1u}}{\partial {}^1\boldsymbol{u}},$$

$$\delta^1 \boldsymbol{u} \cdot \boldsymbol{\mathcal{R}}_2 \equiv \mathcal{R}_{^1u}.$$

For the $(k+1)^{th}$ iteration:

$[^0 \boldsymbol{u}]^{k+1} = [^0 \boldsymbol{u}]^k + [\Delta^0 \boldsymbol{u}]$ – macroscopic displacement jump,

${}^1\boldsymbol{u}^{k+1} = {}^1\boldsymbol{u}^k + \Delta^1 \boldsymbol{u}$ – micro-continuum fluctuation displacement field

$\boldsymbol{t}^{k+1} = \boldsymbol{t}^k + \Delta \boldsymbol{t}$ – macroscopic traction vector

The incrementally linear macroscopic traction-separation law from the linearized form of the macroscopic traction-separation law (by eliminating $\Delta^1 \boldsymbol{u}$),

$$\Delta \boldsymbol{t} = \mathcal{L} : [\Delta^0 \boldsymbol{u}] - \left(\frac{\mathcal{K}_{12}}{\mathcal{K}_{22}}\right)^k : \mathcal{R}_2^k,$$

where,

$$\mathcal{L} = \left(\mathcal{K}_{11} - \frac{\mathcal{K}_{12}}{\mathcal{K}_{22}} \mathcal{K}_{21}\right)^k$$

is the tangent instantaneous cohesive moduli.

2.5. Damage Model

The isotropic damage law is based on irreversible thermodynamics and internal state variables theories. The free energy potential given earlier,

$$\psi({}^A\boldsymbol{\varepsilon}) = \frac{1}{2}({}^0\boldsymbol{\varepsilon} + {}^1\boldsymbol{\varepsilon}) : \mathbb{L} : ({}^0\boldsymbol{\varepsilon} + {}^1\boldsymbol{\varepsilon}) \;\Rightarrow\; \psi({}^A\boldsymbol{\varepsilon}, \omega) = (1-\omega)\psi_0({}^A\boldsymbol{\varepsilon})$$

and

$\psi_0({}^A\boldsymbol{\varepsilon}) = \frac{1}{2} {}^A\boldsymbol{\varepsilon} : {}^A\boldsymbol{L} : {}^A\boldsymbol{\varepsilon}$ – total potential energy function of undamaged material,
ω – isotropic damage parameter,
${}^A\boldsymbol{L}(\boldsymbol{X}, \boldsymbol{Y})$ – elastic stiffness of the micro-constituents.

The 2nd law of thermodynamics for continuum mechanics (neglecting other thermodynamic effects) is the Clausius-Duhem inequality,

$$-\dot{\psi} + \boldsymbol{\tau}:{}^{A}\dot{\boldsymbol{\varepsilon}} \geq 0$$
$$-\dot{\psi} = \frac{d}{dt}[(1-\omega)\psi_0] = (1-\omega)\dot{\psi}_0 - \dot{\omega}\,\psi_0$$
$$\dot{\psi}_0 = \frac{1}{2}\frac{d}{dt}({}^{A}\boldsymbol{\varepsilon}:{}^{A}\boldsymbol{L}:{}^{A}\boldsymbol{\varepsilon}) = \frac{1}{2}\left[{}^{A}\boldsymbol{\varepsilon}\frac{d}{dt}({}^{A}\boldsymbol{L}:{}^{A}\boldsymbol{\varepsilon}) + {}^{A}\boldsymbol{L}:{}^{A}\boldsymbol{\varepsilon}\frac{d}{dt}({}^{A}\boldsymbol{\varepsilon})\right] = \boldsymbol{\tau}:{}^{A}\dot{\boldsymbol{\varepsilon}}$$
$$-\dot{\psi} = (1-\omega)\dot{\psi}_0 - \dot{\omega}(\boldsymbol{\tau}:{}^{A}\boldsymbol{\varepsilon}).$$

which means the dissipative factor is

$$\mathcal{D} = -\dot{\omega}\boldsymbol{Y} \geq 0,$$

where

$$\boldsymbol{Y} = -\psi_0({}^{A}\boldsymbol{\varepsilon})$$

is the damage energy release rate (thermodynamic force) conjugate to the damage variable $\dot{\omega}$. The theory of plasticity contains the concept of yield surface which is analogous to an approach based on damage surface. The damage state in the material is expressed by

$$g(-Y,\chi^{t}) = G(-Y) - \chi^{t} \leq 0$$

with

$t \in \mathbb{R}^{+}$
χ^{t} – softening parameter with the initial value, $\chi^{t=0} = 0$
$G(-Y)$ – characterizes the damage process.

This last function can take on several forms such as a three-parameter Weibull distribution

$$G(-Y) = 1 - \exp\left[-\left(\frac{-Y-Y_{in}}{p_1 Y_{in}}\right)^{p_2}\right],$$

with the three parameters defined:

Y_{in} – energy barrier (units *of* J/m^3 or Pa) for the initial damage threshold
p_1 – non-dimensional **scale** parameter
p_2 – non-dimensional **shape** parameter.

To relate the damage parameter to the damage state, start with the evolution of irreversible dissipation,

$$\dot{\omega} = \dot{\kappa}\frac{\partial g(-Y,\chi^{t})}{\partial(-Y)} = \dot{\kappa}\frac{\partial G(-Y)}{\partial(-Y)}$$

where

$\dot{\kappa}$ – damage loading/unloading parameter with $\{\dot{\kappa} \geq 0\}$ and $\{\dot{\kappa} g(G(-Y), \chi^t) \equiv 0\}$.

$$\frac{\partial G(-Y)}{\partial(-Y)} = \frac{p_2}{p_1 Y_{in}} \left(\frac{(-Y - Y_{in})}{p_1 Y_{in}}\right)^{p_2 - 1} \exp\left(-\left(\frac{(-Y - Y_{in})}{p_1 Y_{in}}\right)^{p_2}\right)$$

To determine $\dot{\kappa}$, the softening parameter evolution also needs to be defined,

$$\dot{\chi}^t = \dot{\kappa} \frac{\partial g(-Y, \chi^t)}{\partial(-Y)} = \dot{\kappa} \frac{\partial G(-Y)}{\partial(-Y)}.$$

Using this definition at a consistency condition (i.e. $\dot{g} = 0$), the following equality is revealed,

$$\dot{g} = -\dot{Y} \frac{\partial G(-Y)}{\partial(-Y)} - \dot{\kappa} \frac{\partial G(-Y)}{\partial(-Y)} = 0,$$

from which,

$$\dot{\kappa} = -\dot{Y}$$
$$\dot{Y} = -\dot{\psi}_e = \boldsymbol{\tau}_e : {}^A\dot{\boldsymbol{\varepsilon}}$$
$$\boldsymbol{\tau}_e = \frac{\boldsymbol{\tau}}{1-\omega}$$
$$\dot{\kappa} = \boldsymbol{\tau}_e : {}^A\dot{\boldsymbol{\varepsilon}}$$

The internal state softening parameter evolution is always the maximum historical value which defined mathematically is,

$$\chi^t = \max\left\{\chi^0, \max_{s \in (-\infty, s]} \chi^s\right\}$$
$$\frac{\partial \chi^t}{\partial t} = \mu(G - \chi^t)$$

The numerical implementation of this may cause biasing towards nodes, which to overcome, it has been proposed to use a viscous damage model with parameter $\phi(g)$ which in a linear viscous damage regime,

$$\phi(g) \equiv \begin{cases} 0, & g > 0 \\ g, & g \leq 0 \end{cases}.$$

2.6. Numerical Implementation

Rate Dependent Damage Integration Algorithm
Note: $\bar{\boldsymbol{Y}} = -\boldsymbol{Y}$

1. Compute: $\bar{\boldsymbol{Y}}_{n+1} = \frac{1}{2} {}^A\boldsymbol{\varepsilon}_{n+1} : {}^A\boldsymbol{L} : {}^A\boldsymbol{\varepsilon}_{n+1}$
2. Check: $g = G(\bar{Y}_{n+1}) - \chi_n$
3. $g > 0$ – No damage occurred, go to Step 5 with $\omega_{n+1} = 0$
4. $g \leq 0$ – Rate dependent damage loading, go to Step 3

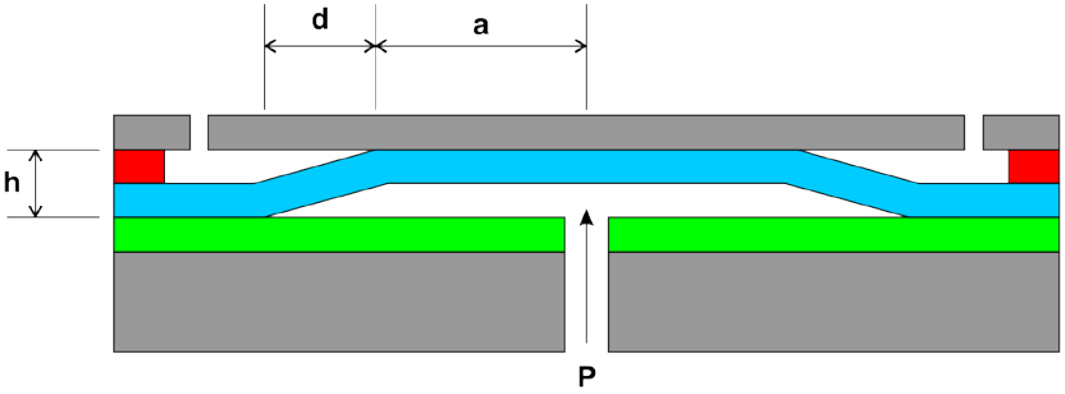

Figure 6. Constrained blister test schematic and dimensions associated with analytical model.

5. Compute: $\omega_{n+1} = \omega_n + \frac{\Delta t}{1+\Delta t\,\mu}[G(\overline{Y}_{n+1}) - \chi_n]$
6. Compute: $\chi_{n+1} = \frac{\chi_n + \Delta t\,\mu\, G(\overline{Y}_{n+1})}{1+\Delta t\,\mu}$
7. Compute: $\tau_{n+1} = (1-\omega_{n+1})\,{}^{A}\boldsymbol{L}:{}^{A}\boldsymbol{\varepsilon}_{n+1}$

2.7. Constrained Blister Test

This test is used to determine the rate at which energy is released in a controlled environment. The controls are used to isolate the fracture energy from other energies in the system such as strain energy from inelastic processes such as plasticity.[7] The image, Figure 6 depicts the critical dimensions of the test and is implemented in an axially symmetric (disk) fashion. The critical dimensions are the height, *h*, which the membrane deflects and the area of delamination, *A*, as a function of time. These dimensions are used to determine the threshold interfacial fracture energy. From this parameter the strain energy release rate can then be determined.

$$\frac{A(t)}{A(t_0)} = \exp\left[\frac{\beta p^2 h}{ph-\gamma}(t-t_0)\right]$$

P – applied pressure relative to atmosphere

γ – Interfacial fracture energy

$$\gamma = (hp)_{\text{threshold}}$$

$P_{\text{threshold}}$ – pressure applied to just cause delamination

β – dissipative coefficient

$$G = ph\left[1 - \frac{d}{2a} + \left(\frac{d}{3a} - \frac{1}{2}\right)\left(\frac{\partial d}{\partial a}\right)\right]$$

G – is the strain energy release rate

3. EXPERIMENTAL AND RESULTS

3.1. Plastic Joining Methods

3.1.1. Adhesive

Multiple types of adhesives were used to join plastics and non-plastics together.[8-13] There are a variety of tapes available for joining nearly any two surfaces including high and low energy surfaces. The most common tape used in these experiments is based on a 3M acrylic-based clean laminating adhesive coated on either a PET or PMMA laminate sheet. The adhesive is 0.5 mil thick and is then converted to the PET or PMMA. Substrates range in thickness from 1.0 mil to 14 mil for PET and greater than 7 mil for PMMA. Other substrates used were Kapton, polycarbonate, Teflon-based materials, paper, glasses/ceramics, and metals.

The sample under test is cut into a particular pattern using CO_2 laser ablation in combination with an XYZ stage and CAD. The adhesive was applied to one side of the adherend and mechanically pressed for 5-600 seconds at pressures ranging from 500 psi to 6000 psi depending on the material. Glasses and other fragile materials were pressed at very low pressures while materials with low-surface energies and rigid materials were pressed at approximately 3000 psi. Surface roughness and topology in combination with adhesive thickness was also a factor in the required pressure for complete bonding with thinner adhesives and rougher surfaces requiring higher pressures.

Figure 3.1.7 shows an image of a device that was fabricated using multiple layers of various thin plastics and adhesives. The plastics included 0.080 inch PMMA, 0.030 inch PMMA, and 0.005 inch PET. The adhesive was 3M brand clean laminating acrylic adhesive, 0.0005 inch, converted (added the poly protective layers) by Fraylock (Valencia, CA). This device had three chambers two of which were filled with liquids and separated from the other chambers by magnetic valves held in place with the same adhesive. In addition, there is a commercially

Figure 7. Image of a laminate device made using adhesives.

available lateral flow assay installed in one of the chambers. Because of the complexity of various materials and overlapping geometries in many layers of this device, and in particular the magnetic/adhesive valves, this system could benefit from a better understanding of the behavior through application of the multiscale model with damage.

From this figure there are defects noted. In particular there are regions of incomplete bonding over the upper right chamber. This defect is due to inadequate support during the bonding process and may affect the long-term bond quality, especially in systems where the chamber may experience a constant internal pressure. The other defect is similar and is located to the far right in the middle and is also a delamination. However, this defect is caused by a trapped unwanted particle. This defect may or may not be readily apparent at first due to the high pressure at which the bond is form. But, because of the high stress caused by the object to the surrounding laminate it will often be a cause of failure. The model may be able to predict the size of particle acceptable and thus determine the rigor of cleanliness required for this operation.

3.1.2. Laser Welding

Using a CO_2 laser and an XYZ stage with a CAD package a pattern was rastered onto the surface of two stacked plastic layers, see Figure 3.1.8. Ideally the top layer is transparent and the bottom later is opaque at the laser wavelength of 10.9 microns. This is not always possible and two relatively transparent materials can still be welded with careful consideration of the laser parameters. The parameters of the laser with total power capability of 60 watts was: 1) Percent power, 2) Percent Speed, 3) points-per-inch, 4) focus, 5) air/gas assist pressure, and 6) vector/raster mode. Materials used were either PEU or PE of thicknesses ranging from 0.0005 inches to 0.004 inches. The PEU was transparent while the PE was either transparent or opaque black in the visible wavelength range.

A sample was prepared by cleaning the bottom and top plastic laminates using isopropanol or

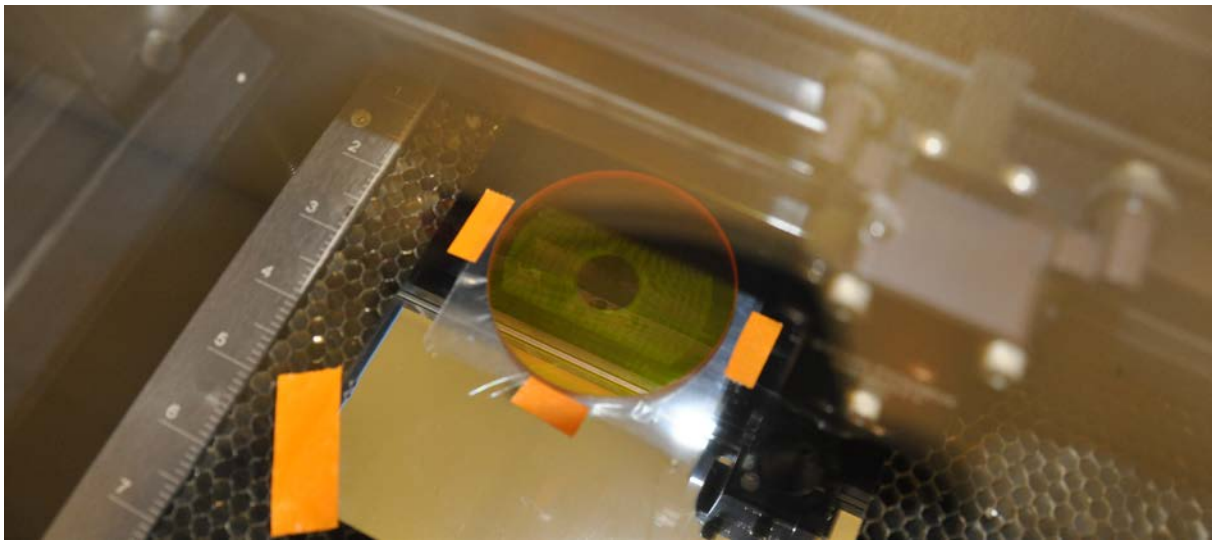

Figure 8. Image of a laminate device made using adhesives. There is a yellow window (ZnSe) on top of the layers being welding. The welded region is indicated by a moiré pattern.

other suitable solvent (methanol, ethanol, and/or water) to remove debris. A small quantity of isopropanol or other solvent was deposited in the center of a polished and flat chrome-coated steel plate. The bottom layer was then put on the drop and pressed flat with a lint-free text wipe, removing all the excess solvent. This fluid helped to hold the bottom layer flat to the surface. The top layer was then cleaned in a similar manner and placed over the bottom layer. The corners and edges were then taped to the metal plate stretching the layer taught. This prestress in the top layer was useful for creating balloon-type cavities for filling with fluid, especially when the bottom layer was thicker and stiffer than the top layer. This method also helped to eliminate wrinkles during the welding processes, which inevitably resulted in holes being laser ablated in the wrinkled regions due to heat not being removed quickly enough in these areas. After taping the top layer in place a thick window of zinc selenide (ZnSe) was placed on top of the two layers to bring them into intimate contact so the welding process was more effective. The ZnSe window was coated to protect the surface since ZnSe is soft and subject to scratches. The coating also allowed for greater transmission of the 10.9 micron wavelength of the laser.

Since each turnkey laser system is unique and the software algorithms carefully guarded, it makes little sense to report the exact raster condition. Ideally, it would be best to report the energy per unit area but this was unknown. These values are typically determined by trial and error and usually can be determined quickly.

An example of a laser welded part is shown in Figure 9. This structure was comprised of two clear 0.004 inch PEU layers. The weld was comprised primarily of bubbles as indicated by the white region. The notch was intentionally designed as a weak point. A test pattern was also fabricated using the same method applied toward the test structure described earlier but with two layers of 0.0009 inch PE layers, both transparent. This was connected to the test setup and both are shown in Figure 10. This weld proved to fail between layers 4 and 5 instead of the desired 5 and 6 and the bond strength was too weak to test. Figure 11 shows the constrained blister test with a replacement of the bottom PE layer with an opaque black 0.002 inch PE layer. This thicker opaque layer allowed the temperature at the interface to reach the critical welding temperature so the chains could intermingle and bond. However, it is clear from these images that the bond was not uniform across the structure and delamination occurred irregularly. The strain energy released between 39 and 51 seconds was estimated around 7.0 joules.

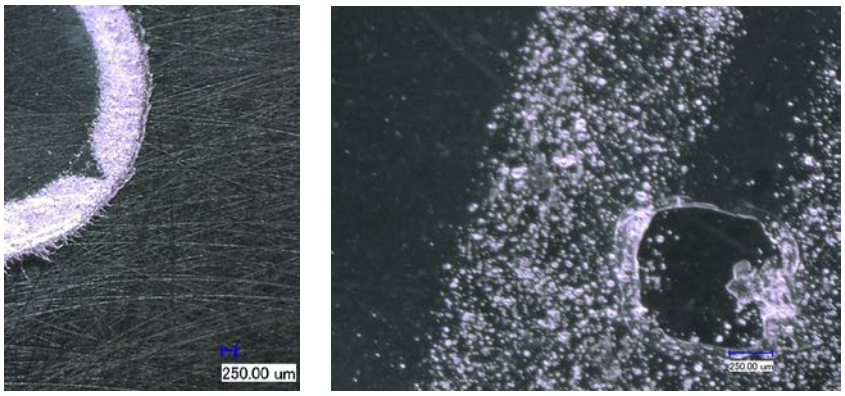

Figure 9. Laser welded joint (white color) in two clear PEU layers. The notch feature provides a weak point. The joint was constituted primarily of bubbles as a result of the welding process.

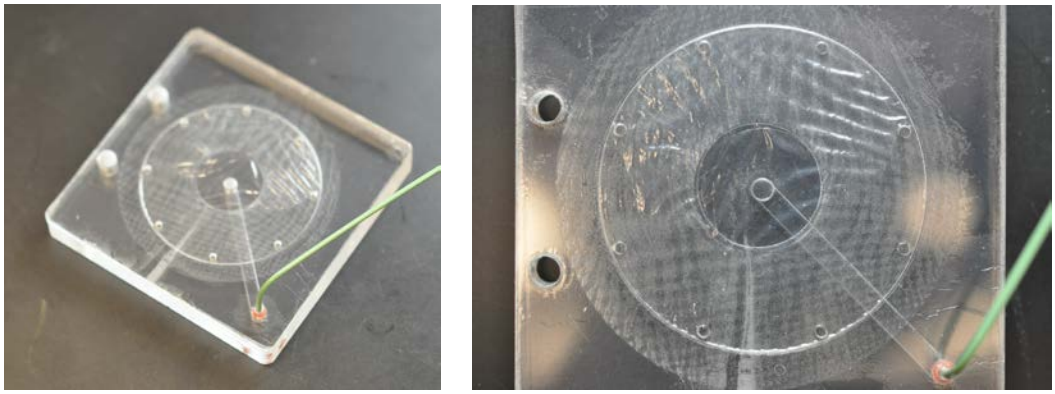

Figure 10. Images of the test structure for the constrained blister test for the laser welded films. The films used in this test were polyethylene.

Figure 11. Results of the constrained blister test as recorded at times 39, 42, 45 and 51 seconds from upper left clockwise. The pattern did not spread uniformly in the radial direction as expected. However, the rate of delamination was still determined by the difference in images and the time between frames.

3.1.3. Solvent Welding

This method is typically reserved for thick materials with relatively short diffusion distances and so may not be appropriate for many of the types of structures typical of microfluidic laminate systems. Additionally, in solvent welding the two materials being joined must be compatible and often cannot be heterogeneous. For example, solvent welding is useful for joining two thick layers of PMMA in a butt joint, edge joint or short overlap joint, Figure 1. In this configuration the diffusion length of the solvent from the innermost point of the joint to the atmosphere is relatively short and a jig can be used to provide the necessary pressure during the welding processes without hampering diffusion. There are many literature resources to show the compatibility matrix of heterogeneous materials in solvent welding.

In Figure 12, the right-most image shows the configuration for a typical laminate structure where the diffusion length is very long. Because the time for the complete removal of this solvent is quite long, the solvent also creates a large diffusion depth into the plastic, nearly the thickness of the plastic in some cases, which in turn destroys any desired structures in the laminate, like channels and valves and such.

The solvents used are typically based on the solvent dichloromethane. Dichloromethane diffuses rapidly into the PMMA or PC and due to its low vapor pressure, evaporates quickly. Other solvent "glues" based on this solvent include high vapor pressure components to slow the diffusion and evaporation so to increase the working time of the material.

A special heated press can also be used to apply the necessary pressure to allow the polymer chains to entangle and also increase the evaporation rate of the solvent.

Using PMMA for solvent welding can be problematic as shown in Figure 13. This image shows a structure similar to the one presented earlier under adhesive joining methods. Along the edge there are stress cracks after solvent welding. These are thick layers of PMMA approximately 0.062 inches. The PMMA was not preshrunk but was laser cut as described. It is believed that the pulsed layer creating a type of serration from localized, periodic stress points due to the intense thermal concentration, and this in combination with the interaction of the solvent causes

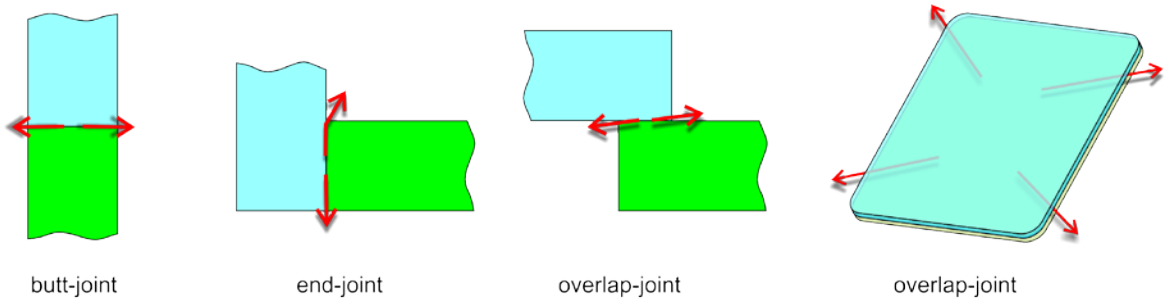

Figure 12. Different joints used in traditional macroscale fabrication are the left three images while that for laminate microscale channel and structure fabrication is shown on the right.

the stress at these locations to intensify and propagate as fractures. Despite these localized fractures the joint proved to be robust and approximate the properties of the raw material itself. The test structure shown in this figure contained blue dyed water and was found to not lose water at any appreciable rate over the period of three months in which it was observed. Bubbles did accumulate near the walls where these fractures were.

It was also very difficult to achieve a uniform bond over a large surface area due to diffusion of the solvent from the inner surfaces and difficulty in uniformly applying a thin solvent to a large area. In Figure 13 there are bubbles trapped between two PMMA layers and are apparent over the dyed water filled region. These defects are expected to reduce bond quality.

3.1.4. Ultrasonic and Other Welding Methods

Ultrasonics are often used to join similar and dissimilar materials. The equipment used is a high power radio frequency source attached to a piezoelectric crystral to provide the ultrasonics. There is typically a horn that focuses the high frequency sound to a particular location on the top surface of the parts to be joined. The sound is transferred to the materials and when hits the interface between the two materials causes vibrations and frictional heating to occur on a microscopic level. The interface then bonds together when the melting temperature of both materials is reached. This is attractive due to the localized joint.

To test the viability of this method for thin materials, several samples of 0.004 inch PET were prepared and sent to a commercial manufacturer to demonstrate the bond-ability of the samples. Also of interest was the area over which the bond could be achieved. The company was chosen based on three decades of experience in the business and manufacturing of ultrasonic welding equipment. They were also the only company at the time to offer a high frequency version of the ultrasonic welder that was in theory more compatible with thinner and more delicate materials. However, all attempts to achieve a weld in such thin materials failed with the destruction of the

Figure 13. Solvent welded structure shows signs of stress cracks at edges and trapped bubbles between layers of PMMA. The structure did successfully contain the liquid with negligible losses for months.

material by melting. It is probable that specialized equipment would be able to achieve the bond necessary but was not pursued here.

Other methods of joining plastics such as RF welding, vibrational welding were not pursued in this work.

3.2. Testing Methods

3.2.1. Unconstrained Blister Test

The blister test (unconstrained) was applied to any of the laminate joining methods using a custom manifold made from both thick and thin layers of plastic as shown in Figure 13. The interface under investigation is integrated into the test structure as layers 5 and 6. The initial area of pressure is defined by an opening cut into layer 5. Each of the layers is adhered to adjacent layers using either solvent welding or adhesive techniques with the exception of the interface between lasers 5 and 6 which is joined by the method under investigation. Layer 7 defined the

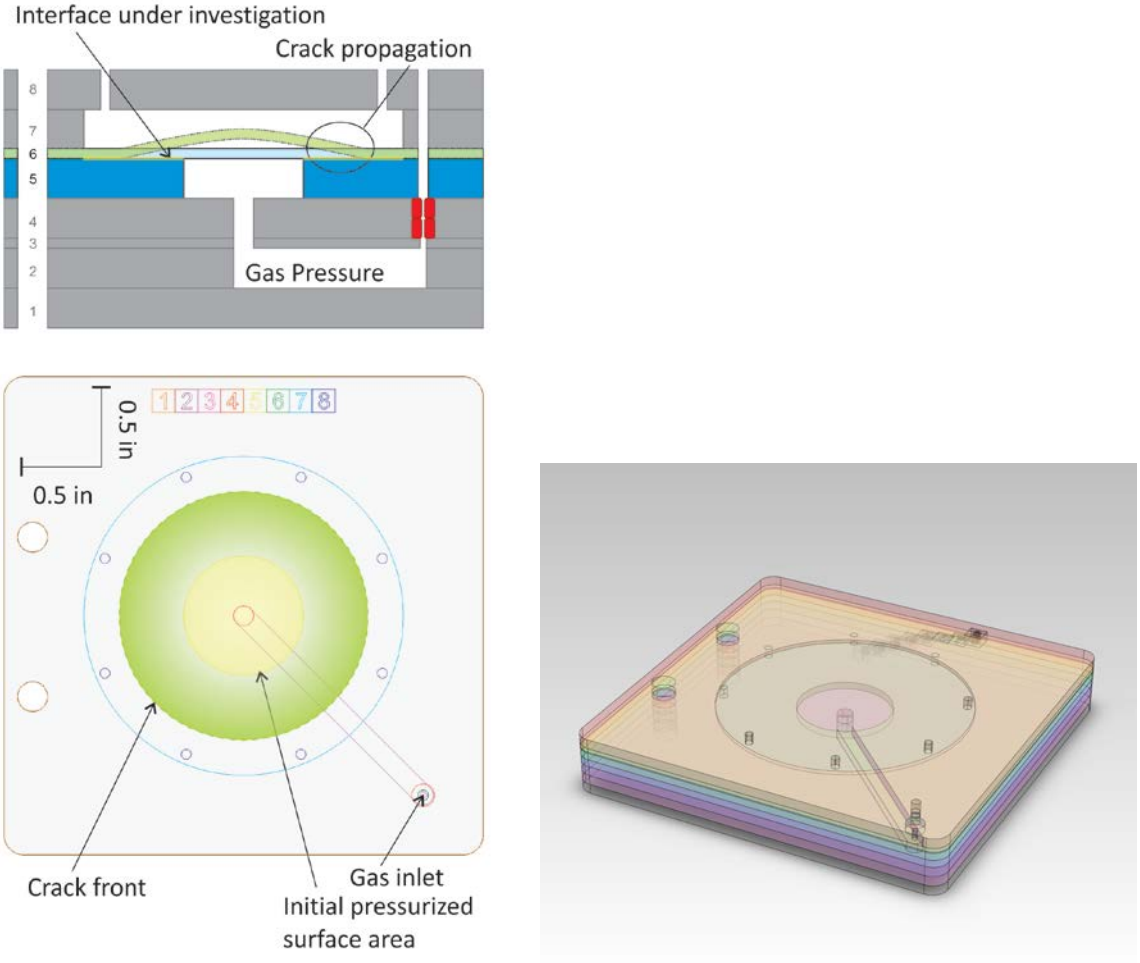

Figure 14. Showing the mechanical envelope of test structure. Top-left image stretched in z-axis direction to show features. Right image shows isometric view of structure to scale.

height between the layer to be stressed and the constrained layer, layer 8. This layer 8 is vented to maintain atmospheric pressure on that side of the test layer. There were no critical alignment features for this test manifold and so rough alignment was accomplished with two pins in a fixture. Each layer had alignment holes cut into the pattern.

3.2.2. Constrained Blister Test

To convert the unconstrained blister to a constrained blister test only layer 7 of the test manifold was required to be modified. For the unconstrained test the thickness of layer 7 used was 0.062 inches. For the constrained blister test the thickness of layer 7 was reduced to 0.005 inches. Because of the precision and accuracy of making plastic films, the commercially available optional thicknesses of this layer included 0.5, 0.9, 1.0, 1.5, 2.0 to 14.0, 20 to 60 mils, and combinations of these thickness to achieve nearly any thickness necessary. The setup for the constrained blister test is shown in Figure 15.

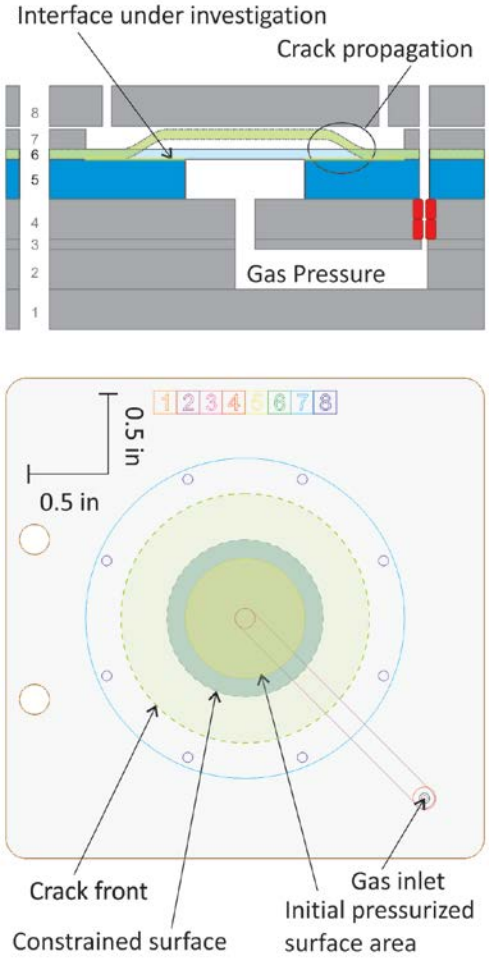

Figure 15. Constrained blister test manifold mechanical envelope shown. Layer 7 was reduced to prevent elastic processes in layer 6 and confine all energy released to the interfacial delamination.

3.2.3. Test Setup

Gas pressure is applied to this area by insertion of 1/16 inch OD PEEK tubing into the O-ring. The house nitrogen pressure source is connected to the tubing and a pressure transducer as shown in Figure 16. The pressure transducer was kept at the same height to eliminate head pressure offsets. An Omega PX-280 pressure transducer was used and was connected to a National Instruments USB-DAQ. The NI DAQ supplied the power and acquired the analog signal. A custom computer program interfaced with the DAQ unit to start acquisition and display the data in graphical format and save the raw data to a text file. The Microsoft Visual Studio C# computer program is detailed in Appendix B. Tubing was obtained from Upchurch Scientific.

A Nikon D90 digital camera with Nikkor 60mm macro lens was use to acquire images on a timed basis. This was accomplished with the camera's on-board timed image acquisition function and subsequent transfer of images to the computer, or with a computer data cable and Nikon's Cameral Control software which also allows for timed acquisition of images which are stored directly on the computer. The first image time was noted with respect to the computer's pressure data log time and subsequent images were aligned accordingly.

The setup was very fast to assemble and begin taking data. The longest part of the process was preparing the interface to be investigated. The manifold was disposable and took approximately and hour to prepare. In addition, the cost of materials for the manifold was approximately a few USD or less.

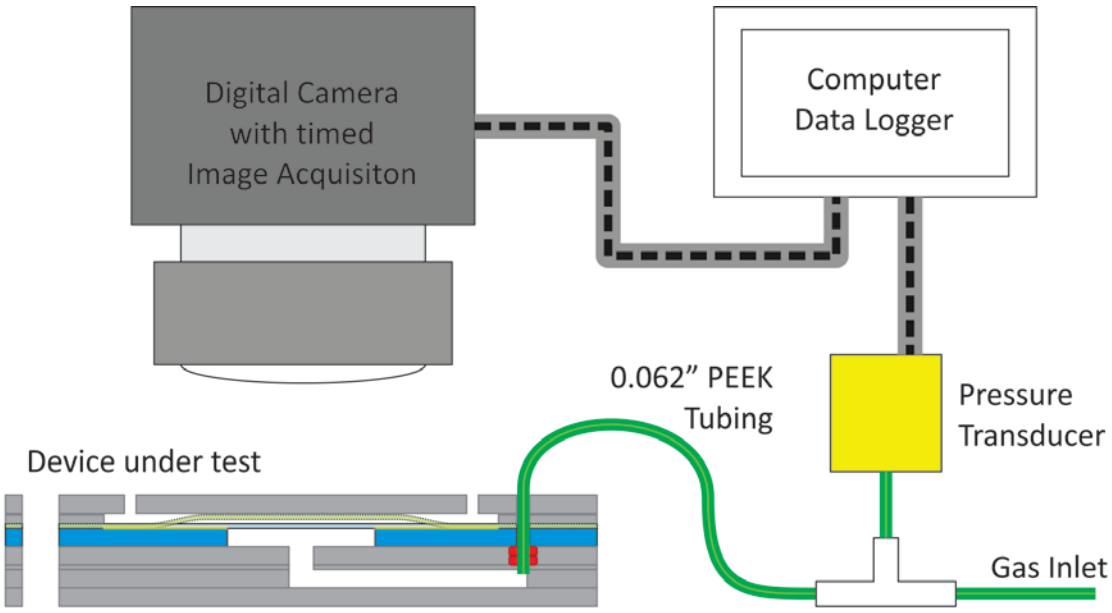

Figure 16. Pressure setup for blister and constrained blister tests including a pressure transducer and camera for data generation and computer for data acquisition, reporting, and storage. Not shown is the digital to analog converter and power supply in between the computer and pressure transducer.

3.2.4. Blister Test Operation

The sample layers were prepared according to the desired method as described earlier. The other layers of the test manifold were cut out with the laser and were assembled in no particular order except that the test structure was joined lastly with the layers 1 through 4 and layer 8.

The nitrogen gas pressure was adjusted to zero and the shut-off valve turned off. The differential pressure was verified to be at zero. The end of the tubing was plugged, the shut-off valve was opened, and the pressure regulator adjusted so that the computer displayed the desired pressure. The shut-off valve was closed and the tubing was inserted into O-rings of the manifold.

The camera was positioned perpendicular to the top of the test manifold so that the entire manifold was in the field of view and secured to the bench with tape. The timing of images was set to the desired interval. This interval was set based-on the velocity of the delaminating front as observed from previous experiments. The logging function of the pressure program was started followed by starting the image sequence acquisition. The datalog time at which the first image was acquired was noted. The shut-off valve was opened and the time noted.
After the delamination terminates to the edge of the test structure the shut-off valve is closed and all systems are stopped.

4. CONCLUSIONS

The purpose of this work was to discover a method to investigate the properties of interfaces as described by a numerical physical model. The model used was adopted from literature and applied to a commercially available multiphysics software package. By doing this the internal properties of simple structures could be elucidated and then readily applied to more complex structures such as valves and pumps in laminate microfluidic structures.

To achieve the goals of this project however, methods of joining the laminates of various materials was required to be established. Several methods were investigated such as adhesives, solvent welding, laser welding, and ultrasonic welding. The adhesive method was the most successful and easy to implement but also one of the more difficult to understand, especially over long periods of time. Welding methods are meant to achieve a bond that is similar to bulk properties and so are easier to predict. However, methods of welding often produce defects in the bonds.

These defects and complex adhesives require a physical model that is heterogeneous on the microscale. This presents complications for numerical models due to the multiple scales over which the structures are being investigated. Again literature has aided in the solution of this and the model used included a repetitive volume element and multiscale model to reduce the computing power required.

Examples of the test structures used to elucidate the internal properties of the model were shown and demonstrated. The real life examples used this research to improve upon current designs and aided in creating complex structures for sensor and other applications.

5. REFERENCES

1. K. Matous, M.G. Kulkarni, P.H. Geubelle, *Multiscale cohesive failure modeling of heterogeneous adhesives*, J. of the Mechanics and Physics of Solids, 56 (2008) 1511-1533.
2. A. Tatone, *Mechanics of Solids and Materials*: Elastic affine bodies, DISAT, University of L'Aquila, (2011) 933.
3. D. Cousineau, *Fitting the Three-Parameter Weibull Distribution: Review and Evaluation of Existing and New Methods*, Universite de Montreal, Montreal, Quebec, Canada, internet link.
4. X. Li, X. Zhang, J. Zhang, *A generalized Hill's lemma and micromechanically based macroscopic constitutive model for heterogeneous granular materials*, Comput. Methods Appl. Mech. Engrg. 199 (2010) 3137-3152.
5. Y. Yamamoto, *An intrinsic theory of a Cosserat continuum*, Int. J. Solids Structures, 4 (1968), 1013-1023.
6. C. Miehe, J.Schroder, M. Becker, *Computational homogenization analysis in finite elasticity: material and structural instabilities on the micro- and macro-scales of periodic composites and their interaction*, Comput. Methods Appl. Mech. Engrg. 191 (2002) 4971-5005.
7. R. Lacombe, *Adhesion measurements methods*, CRC Press, Boca Raton, FL (2006), 27-31 (and in general all theory presented through the book).
8. S.E. Nielsen, J.K. Kristensen, M. Strange, *Laser Welding of Plastics – Weld Compatibility Investigations*, FORCE Technology, Brondby, Denmark, internet link.
9. J.Y. Cheng, C.W. Wei, K.H.Hsu, T.H. Young, *Direct-write laser micromachining and universal surface modification of PMMA for device development*, Sensors and Actuators B 99 (2004), 186-196.
10. J.Y. Cheng, M.H. Yen, C.T. Kuo, T.H. Young, *A transparent cell-culture microchamber with a variably controlled concentration gradient generator and flow field rectifier*, Biomicrofluidics, 2 (2008).
11. H. Klank, J.P. Kutter, O. Geschke, *CO2-laser micromachining and back-end processing for rapid production of PMMA-based microfluidic systems*, Lab Chip, 2, 242246 (2002).
12. R.P. Wool, B.L. Yuan, O.J. Mcgarel, *Welding of Polymer Interfaces*, Polymer Engineering and Science, 29, 19 (1989).
13. W.W. Duley, R.E. Mueller, *CO2 laser welding of polymers*, Polymer Engineering and Science, 32, 9 (1992), 582-584.

APPENDIX A: COMSOL IMPLEMENTATION OF MODEL

Paper.mph
Date
Sep 8, 2012 3:49:39 PM
Contents

1. Global Definitions
1.1. Parameters 1
Parameters

Name	Expression	Description
radius	40e-6[m]	
thick	300 [um]	
p1	100	
p2	1	
YinM	0.10 [J/m^3]	
YinI	0.35 [J/m^3]	
rhoI	1 [kg/m^3]	
rhoM	1000 [kg/m^3]	
nuB	0.34	
EM	2.4e9 [Pa]	
EI	0.8e9 [Pa]	
mut	19 [1/s]	
displacement	0.001 [mm]	
rate	0.1 [1/s]	

2. Model 1 (mod1)

2.1. Definitions

Variables

Variables Matrix

Selection

Geometric entity level	Domain
Selection	Domain 1

Name	Expression	Description
Yb	solid.Ws	
R1	((Yb/YinM-1)/p1)^p2	
G	1-exp(-R1)	

Variables Inclusions

Selection

Geometric entity level	Domain
Selection	Domains 2-41

Name	Expression	Description
Yb	solid.Ws	
R2	((Yb/YinI-1)/p1)^p2	
G	1-exp(-R2)	

Probes

Domain Probe 1

Probe type Domain probe

Domain Probe 2

Probe type Domain probe

Model couplings

Maximum 1

Coupling type	Maximum
Operator name	maxop1

Selections

Explicit 1

Selection

Boundary 6

Coordinate systems

Boundary System 1

Coordinate system type	Boundary system
Identifier	sys1

2.2. Geometry 1

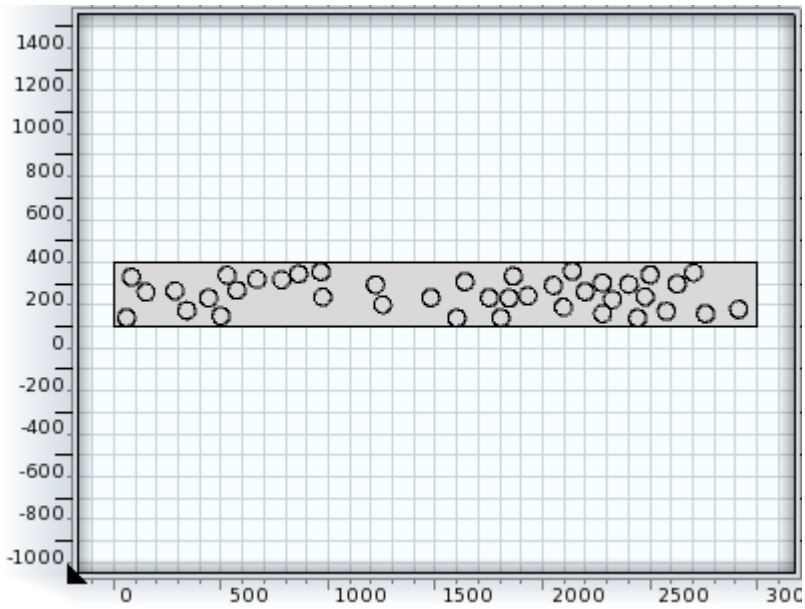

Geometry

2.3. Materials

Matrix

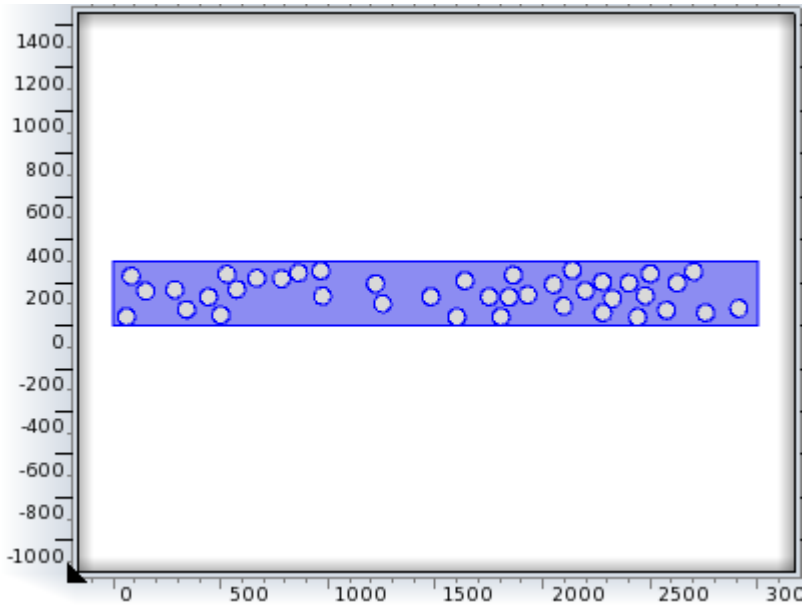

Matrix

Selection

Geometric entity level	Domain
Selection	Domain 1

Inclusions

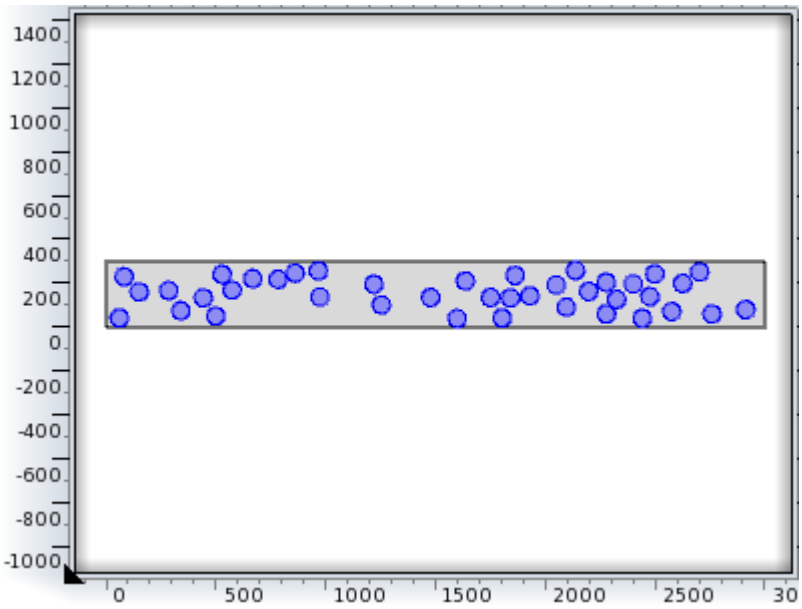

Inclusions

Selection

Geometric entity level	Domain
Selection	Domains 2-41

2.4. Solid Mechanics (solid)

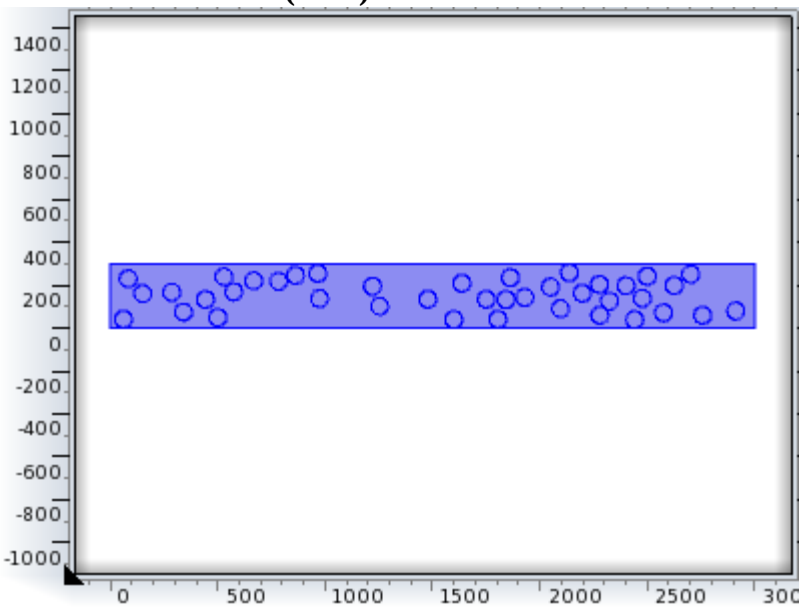

Solid Mechanics

Features

Linear Elastic Material Model 1

Free 1

Initial Values 1

Fixed Constraint 1

Periodic Condition 1

Prescribed Velocity 1

2.5. Xt ODE (dode)

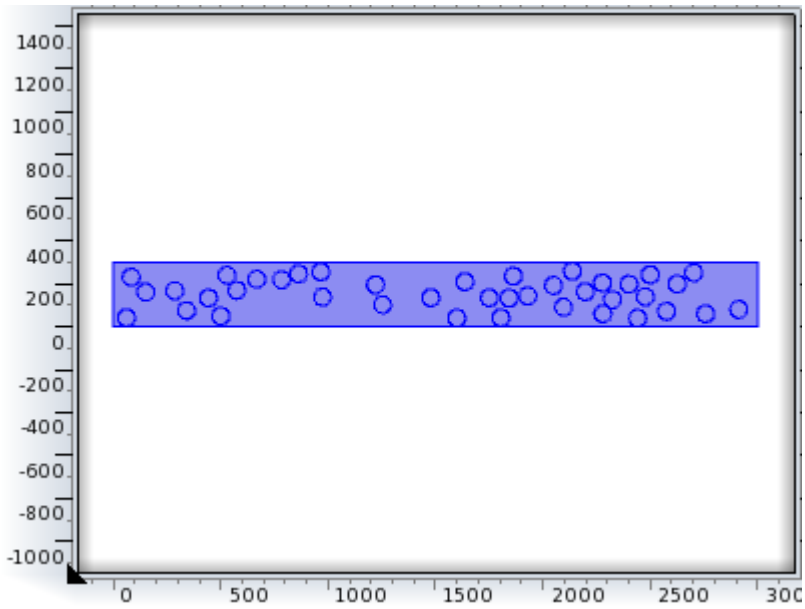

Xt ODE

Features

Distributed ODE 1

Initial Values 1

2.6. W ODE (dode2)

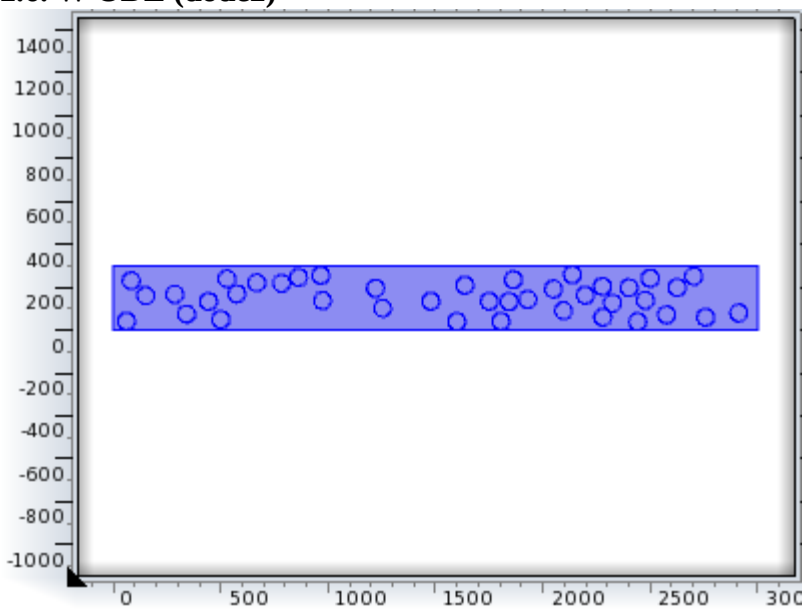

W ODE

Features

Distributed ODE 1

Initial Values 1

2.7. Mesh 1

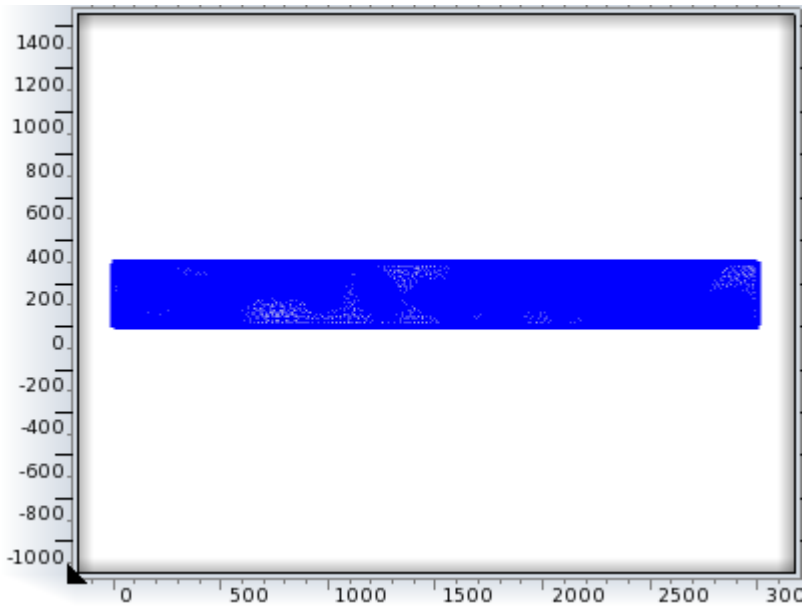

Mesh 1

3. Study 1

3.1. Time Dependent

Times: range(0,0.001,1)

Mesh selection

Geometry	**Mesh**
Geometry 1 (geom1)	mesh1

Physics selection

Physics interface	**Discretization**
Solid Mechanics (solid)	physics
Xt ODE (dode)	physics
W ODE (dode2)	physics

4. Results

4.1. Data Sets

Solution 1

Selection

Geometric entity level	Domain
Selection	Geometry geom1

Settings

Name	**Value**
Solution	Solver 1
Model	Geometry 1

Probe Solution 2

Selection

Geometric entity level	Domain
Selection	Geometry geom1

Settings

Name	**Value**
Solution	Solver 1
Model	Geometry 1

Domain Probe 1
Selection
Geometric entity level Domain
Selection Domains 2-41
Settings

Name	Value
Data set	Probe Solution 2
Method	Integration
Integration order	on

Domain Probe 2
Selection
Geometric entity level Domain
Selection Domain 1
Settings

Name	Value
Data set	Probe Solution 2
Method	Integration
Integration order	on

4.2. Derived Values
Surface Average 1
Selection
Geometric entity level Domain
Selection Domains 2-41
Settings

Name	Value
Data set	Solution 1
Expression	Xt1
Description	Dependent variable Xt1
Parameters	{{solid.refpntx, 0, Reference point for moment computation, x component}, {solid.refpnty, 0, Reference point for moment computation, y component}, {solid.refpntz, 0, Reference point for moment computation, z component}}

Surface Average 2
Selection
Geometric entity level Domain
Selection Domains 1-41
Settings

Name	Value
Data set	Solution 1
Expression	solid.mises
Unit	N/m^2
Description	von Mises stress
Parameters	{{solid.refpntx, 0, Reference point for moment computation, x component}, {solid.refpnty, 0, Reference point for moment computation, y component}, {solid.refpntz, 0, Reference point for moment computation, z component}}

Domain Probe 1
Settings

Name	Value
Data set	Domain Probe 1
Time selection	manual
Time	984
Expression	Xt1
Description	Dependent variable Xt1
Parameters	{{solid.refpntx, 0, Reference point for moment computation, x component}, {solid.refpnty, 0, Reference point for moment computation, y component}, {solid.refpntz, 0, Reference point for moment computation, z component}}

Domain Probe 2

Settings

Name	Value
Data set	Domain Probe 2
Time selection	manual
Time	984
Expression	Xt1
Description	Dependent variable Xt1
Parameters	{{solid.refpntx, 0, Reference point for moment computation, x component}, {solid.refpnty, 0, Reference point for moment computation, y component}, {solid.refpntz, 0, Reference point for moment computation, z component}}

Line Integration 1

Selection

Geometric entity level	Boundary
Selection	Boundary 3

Settings

Name	Value
Data set	Solution 1
Expression	solid.Tay
Unit	N/m
Description	Surface traction (force/area), y component
Parameters	{{solid.refpntx, 0, Reference point for moment computation, x component}, {solid.refpnty, 0, Reference point for moment computation, y component}, {solid.refpntz, 0, Reference point for moment computation, z component}}

Surface Integration 2

Selection

Geometric entity level	Domain
Selection	Domains 1-41

Settings

Name	Value
Data set	Solution 1
Expression	solid.Ws
Unit	N
Description	Strain energy function
Parameters	{{solid.refpntx, 0, Reference point for moment computation, x component},

{solid.refpnty, 0, Reference point for moment computation, y component},
{solid.refpntz, 0, Reference point for moment computation, z component}}

4.3. Tables

Table 1

Surface Average 2 (solid.mises)

Table was not included due to space constraints.

Probe Table 2

Table 3

Line Integration 1 (solid.Tay)

Table was not included due to space constraints.

Table 4

Surface Integration 2 (solid.Ws)

Table was not included due to space constraints.

4.4. Plot groups

Stress (solid)

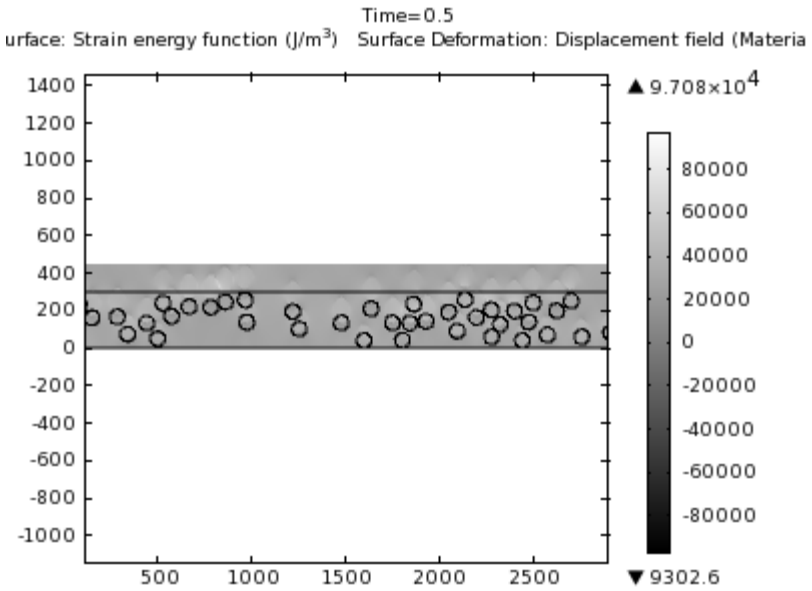

Time=0.5 Surface: Strain energy function (J/m^3) Surface Deformation: Displacement field (Material)

2D Plot Group 2

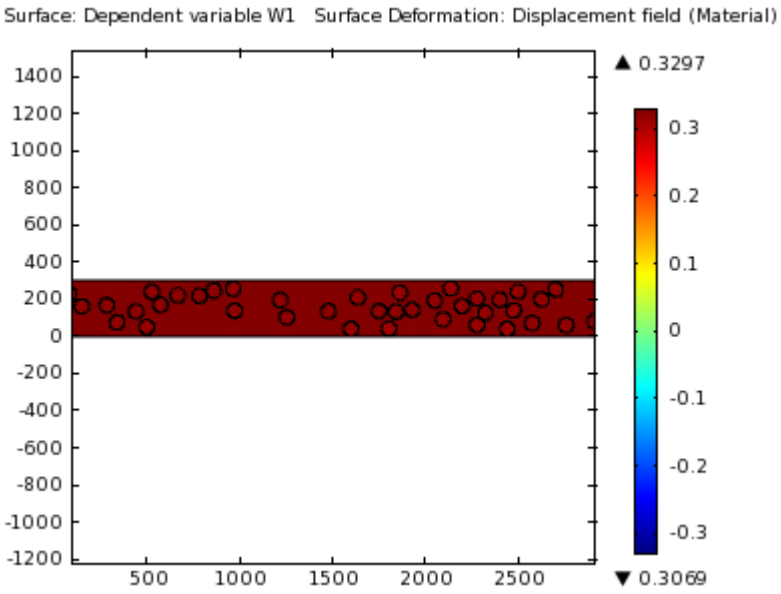

Surface: Dependent variable W1 Surface Deformation: Displacement field (Material)

2D Plot Group 3

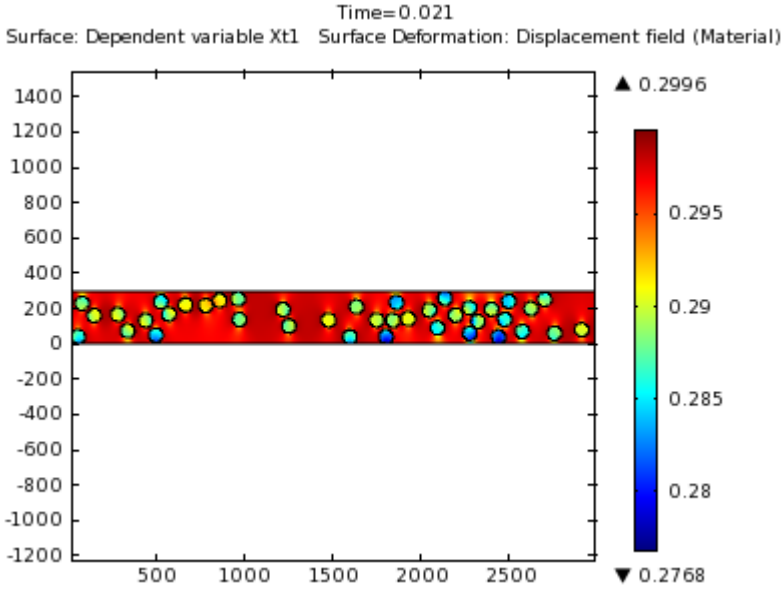

Time=0.021 Surface: Dependent variable Xt1 Surface Deformation: Displacement field (Material)

Probe 1D Plot Group 4

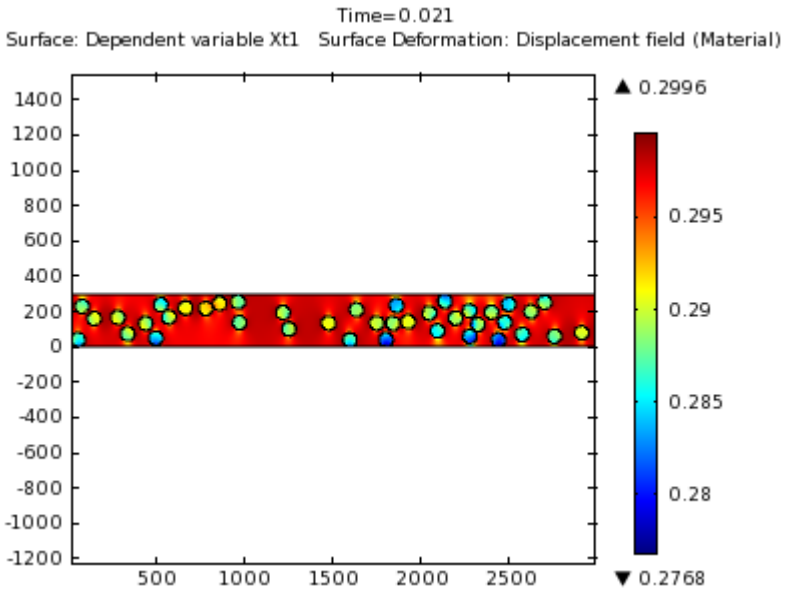

1D Plot Group 5

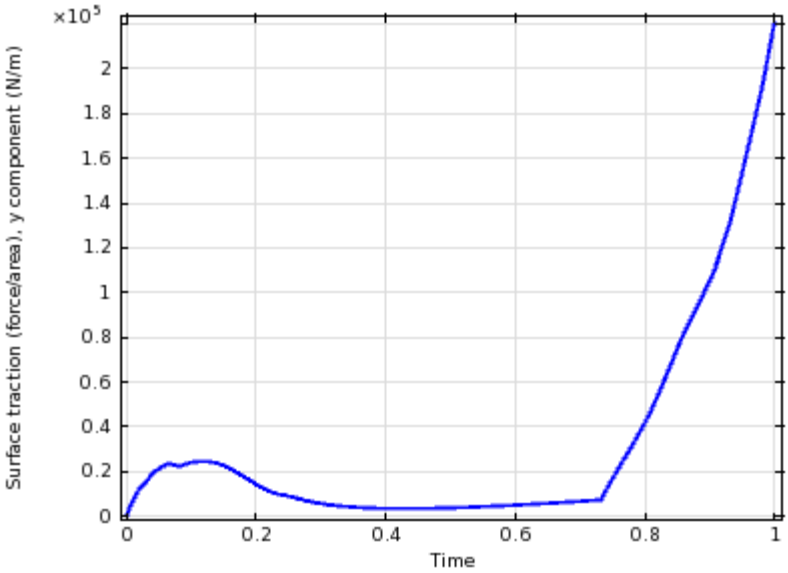

1D Plot Group 6

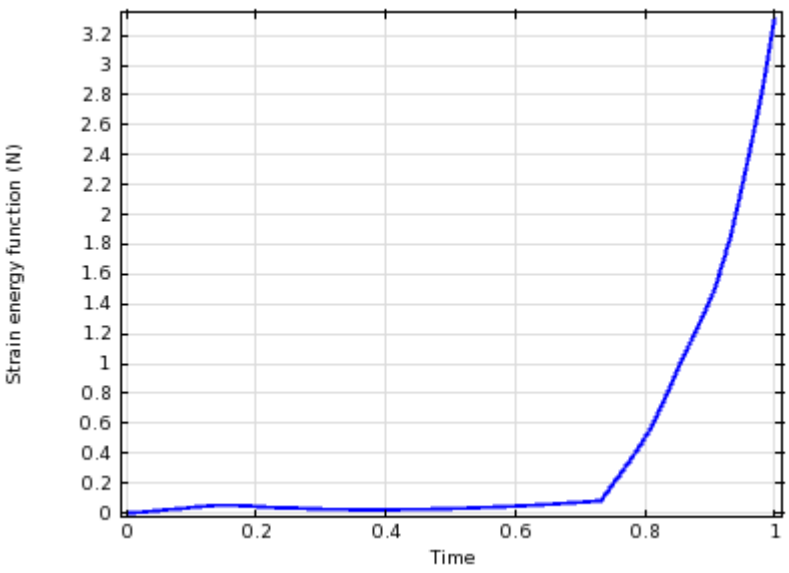
Strain energy function (N)
Time
0
0.2
0.4
0.6
0.8
1
0.2
0.4
0.6
0.8
1
1.2
1.4
1.6
1.8
2
2.2
2.4
2.6
2.8
3
3.2

Appendix B: Visual C# Program for Pressure Acquisition

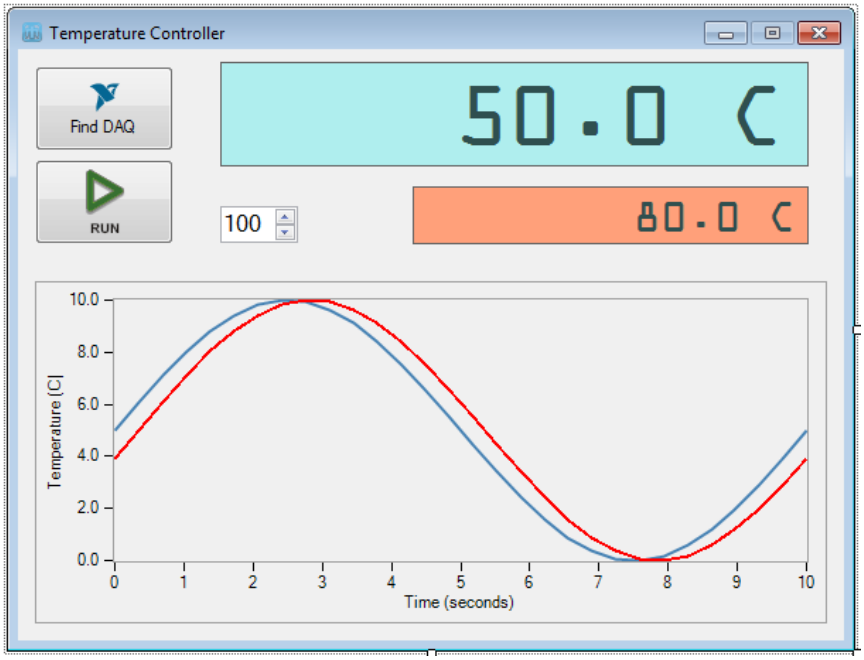


```
using NationalInstruments;
using NationalInstruments.DAQmx;
using NationalInstruments.UI;
using NationalInstruments.UI.WindowsForms;
using System;
using System.Collections.Generic;
using System.ComponentModel;
using System.Data;
using System.Drawing;
using System.Linq;
using System.Text;
using System.Windows.Forms;

namespace Pressure_Indicator
{
    public partial class Form1 : Form
    {

        #region Declarations of Constants and Variables

        //  National Instruments
        private Task daqTask;
        private Device daqDevice;
        private string daqDeviceName;
        private AnalogMultiChannelReader daqReader;
        private string[] daqAIs;
        private string[] daqCOs;

        //  Other
```

```
        private double[,] daqData = null;
        private double tempA;
        private double tempSP;
        private double voltage;
        private const int numData = 100;

        #endregion

        public Form1()
        {
            InitializeComponent();
        }

        private string daqFinder()
        {
            try
            {
                foreach (string daq in DaqSystem.Local.Devices)
                {
                    daqDevice = DaqSystem.Local.LoadDevice(daq);
                    daqDeviceName = daqDevice.ProductCategory + " : " +
                        daqDevice.ProductType + " : " + daqDevice.ProductNumber;
                    daqAIs = daqDevice.GetPhysicalChannels
                        (PhysicalChannelTypes.AI, PhysicalChannelAccess.External);
                    daqCOs = daqDevice.GetPhysicalChannels
                        (PhysicalChannelTypes.CO, PhysicalChannelAccess.External);
                    if (daqCOs.Length > 0 & daqAIs.Length > 0)
                    {
                        DialogResult useDAQ = MessageBox.Show("Do you want to use this
device?",
                            daqDeviceName, MessageBoxButtons.YesNo,
MessageBoxIcon.Question);
                        if (useDAQ == DialogResult.Yes)
                        {
                            return daqDevice.ProductType;
                        }
                    }
                    daqDevice.Dispose();
                }
                MessageBox.Show("Not Found", "No suitable NI-DAQ found",
                    MessageBoxButtons.OK, MessageBoxIcon.Hand);
                daqDevice.Dispose();
                return "Find DAQ";
            }
            catch (DaqException de)
            {
                MessageBox.Show(de.Message);
            }
            return "Find DAQ";
        }

        private void setupChannels()
        {
            daqTask = new Task();
            daqTask.AIChannels.CreateVoltageChannel(daqAIs[0], "Temperature",
                AITerminalConfiguration.Differential, -10, 10, AIVoltageUnits.Volts);
            daqTask.AIChannels.CreateVoltageChannel(daqAIs[1], "Five Volts",
                AITerminalConfiguration.Differential, -10, 10, AIVoltageUnits.Volts);
```

```
        daqTask.COChannels.CreatePulseChannelFrequency(daqCOs[0], "PWM",
            COPulseFrequencyUnits.Hertz, COPulseIdleState.Low, 0, 100, 50);

        daqTask.Control(TaskAction.Verify);

        daqReader = new AnalogMultiChannelReader(daqTask.Stream);

    }


    private void buttonDAQ_Click(object sender, EventArgs e)
    {
        buttonDAQ.Text = daqFinder();
        setupChannels();
    }

    private void buttonRunStop_Click(object sender, EventArgs e)
    {
        if (buttonRunStop.ImageIndex == 0)
        {
            buttonRunStop.ImageIndex = 1;
            timerDAQ.Enabled = true;
            timerDAQ.Start();

            waveformGraph_Temperature.ClearData();
            daqData = new double[2, numData];
        }
        else
        {
            buttonRunStop.ImageIndex = 0;
            timerDAQ.Stop();
            timerDAQ.Enabled = false;
        }
    }

    private void timerDAQ_Tick(object sender, EventArgs e)
    {
        //Acquire data
        tempA = 0;
        voltage = 0;

        daqData = daqReader.ReadMultiSample(numData);
        for (int i = 0; i < numData; i++) {tempA += daqData[0, i];}
        tempA = tempA / numData;
        voltage = voltage / numData;

        //Calculate temperature, 10 millivolts per degree C
        tempA = tempA / 0.01;

        //Plot data
        waveformGraph_Temperature.PlotYAppend(tempA);

        //Diplay data
        label_TempA.Text = tempA.ToString("F1") + " C";
    }

    private void Form1_FormClosed(object sender, FormClosedEventArgs e)
    {
```

```
            try{daqTask.Dispose();}
            catch { };
        }

        private void Form1_Load(object sender, EventArgs e)
        {

        }


    }
}
```

DISTRIBUTION

1	MS0892	Thayne L. Edwards	01714
1	MS1425	Steve Casalnuovo	01714
1	MS0899	Technical Library	9536 (electronic copy)
1	MS0359	D. Chavez, LDRD Office	1911


Sandia National Laboratories